SCIENCE CHINA
Information Sciences

• RESEARCH PAPER •

August 2026, Vol. 69, Iss. 8, 182301:1–182301:15
https://doi.org/10.1007/s11432-025-4779-6

Movable array based design for beam squint suppression in THz IRS communications

Yanze ZHU[1], Qingqing WU[1*], Wen CHEN[1], Yang LIU[2,3],
Wanming HAO[4] & Derrick Wing Kwan NG[5]

[1]*Department of Electronic Engineering, Shanghai Jiao Tong University, Shanghai 200240, China*
[2]*School of Information and Communication Engineering, Dalian University of Technology, Dalian 116024, China*
[3]*National Mobile Communications Research Laboratory, Southeast University, Nanjing 211111, China*
[4]*School of Electrical and Information Engineering, Zhengzhou University, Zhengzhou 450001, China*
[5]*School of Electrical Engineering and Telecommunications, University of New South Wales, Sydney NSW 2052, Australia*

Received 30 June 2025/Revised 22 October 2025/Accepted 29 January 2026/Published online 8 July 2026

Abstract In this paper, we study an intelligent reflecting surface (IRS)-aided wideband terahertz (THz) multiple-input-single-output (MISO) communication system, where the base station (BS) is equipped with movable antennas (MAs) and the IRS consists of movable subarrays. To alleviate the double beam squint effect caused by the coupling of the beam squint at the BS and IRS, we propose to maximize the minimum received power across a wide THz spectrum by optimizing the MAs' and IRS subarrays' positions. This task is highly challenging due to the max-min form objective and nonconvex constraints for avoiding antenna coupling and subarray collision. By adopting the majorization-minimization (MM) methodology, we develop an algorithm to tackle the aforementioned challenge. Numerical results demonstrate the effectiveness of our proposed algorithm and verify the benefits of utilizing the movable components embedded in the BS and IRS to mitigate the double beam squint effect in the considered THz wideband system.

Keywords terahertz (THz) communication, movable antenna (MA), intelligent reflecting surface (IRS), double beam squint effect, joint position optimization

Citation Zhu Y Z, Wu Q Q, Chen W, et al. Movable array based design for beam squint suppression in THz IRS communications. Sci China Inf Sci, 2026, 69(8): 182301, https://doi.org/10.1007/s11432-025-4779-6

1 Introduction

1.1 Background

Terahertz (THz) communication has emerged as a promising technology for next-generation wireless networks [1]. Thanks to its high bandwidth, it is suitable for many applications, such as high-speed data transfer, imaging, and security scanning. With the growing demand for faster communication, THz communication is envisioned to play a crucial role in advancing mobile broadband, enabling low-latency communications, and facilitating Internet-of-Things (IoT) networks [2]. However, in practice, its deployment is constrained by severe path loss and atmospheric absorption, significantly limiting its potential.

To overcome this drawback, the intelligent reflecting surface (IRS) has attracted great attention from both academia and industry as a promising technology for enhancing THz communication performance [3]. IRS consists of advanced material surfaces equipped with numerous low-cost passive reflecting elements that can intelligently manipulate the wireless signal propagation environment. By adjusting the phase of reflected signals, IRS can create favorable communication channels, thereby improving coverage, capacity, and energy efficiency (EE). The potential of IRS has been greatly explored in [4–12]. For instance, the authors in [4] uncovered that the transmit power at the base station (BS) can be reduced with IRS assistance. By appropriately configuring the IRS, the N^2 power scaling law was achieved, with N being the number of IRS elements, significantly outperforming traditional multiple-input-multiple-output systems without IRS. Meanwhile, Ref. [5] considered energy-efficient multiuser communication by deploying an IRS. After solving an EE maximization problem by optimizing IRS phase shifts, the system's EE improved significantly. In [6], a simultaneously wireless information and power transfer system aided by IRSs was

* Corresponding author (email: qingqingwu@sjtu.edu.cn)

© Science China Press 2026

proposed. The study verified that wireless power harvesting can be significantly enhanced by using an IRS. The authors in [7] proposed the use of IRS in an orthogonal frequency division multiplexing (OFDM) system. By delicately designing a transmission protocol for the IRS-assisted OFDM system, the communication rate can be dramatically boosted while maintaining a low training overhead. Meanwhile, Ref. [8] accounted for the nonorthogonal multiple access (NOMA) scenario and demonstrated that the deployment of IRS can enable power-efficient communication. In [9], an IoT network with an IRS was studied; by jointly optimizing the IRS configuration and transmission time allocation, the system's sum-throughput was increased by 100% compared with the scheme without an IRS. The authors in [10, 11] introduced the IRS into integrated sensing and communication (ISAC) systems. In particular, as demonstrated in [11], leveraging the IRS improved the security of the ISAC system while guaranteeing both communication and sensing quality. Moreover, a recent study [12] found that, deploying IRSs at appropriate positions can significantly improve performance. More importantly, as elaborated in [12], given an identical number of IRS elements, the distributed deployment of multiple IRSs is superior to the centralized deployment of a single IRS under specific conditions.

Thanks to its versatility, as explored in the existing literature, some researchers have proposed using IRS to enhance the performance of THz communication [13–19]. Specifically, the authors in [13] considered improving the sum-rate of a THz communication system using an IRS. By embedding a few time delay modules into the IRS and adjusting their phase shifts, the transmission rate was significantly increased. Ref. [14] extended the idea presented in [13] to a near-field (NF) scenario and demonstrated that, by developing a double-layer delta-delay architecture for the IRS, the array gain and achievable rate were remarkably boosted. In [15], a cooperative beam training scheme was proposed for channel estimation in IRS-aided THz communication, and a hybrid beamforming strategy was designed based on the training results. The sum-rate of the considered THz communication system was significantly improved by using an IRS. Ref. [16] accounted for the imperfect channel state information (CSI) and presented a robust hybrid beamforming scheme to enhance data transmission in a THz communication system with an IRS. The authors in [17] studied the impact of different IRS sizes, shapes, and deployments on beam squint. Accordingly, they developed a hybrid beamforming scheme that exploits time delays at the BS to maximize the achievable rate for THz communication. Ref. [18] addressed the severe propagation attenuation that occurs in THz communication systems by deploying multiple IRSs. By adopting deep reinforcement learning to maximize the ergodic sum-rate, the coverage range of THz communication was increased by 50% relative to its conventional counterpart. In [19], a THz communication system aided by multiple IRSs was proposed; the authors demonstrated that by carefully placing IRSs within the system and leveraging a codebook-based three-dimensional beam scanning approach, the average sum-rate can be significantly improved.

Another promising technology recently proposed is the movable antenna (MA) [20]. It represents a significant advancement in wireless communications, enabling dynamic adaptation to varying operational environments. Unlike traditional fixed-position antennas (FPAs), MAs can be repositioned to optimize signal coverage, enhance communication reliability, and improve data throughput using the liquid metal technique [21] or stepper motors [22]. Their versatility makes them suitable for a range of applications, including mobile telecommunications, disaster recovery, and military communications, where rapid deployment and adaptability are crucial. A growing body of research has concentrated on exploring the potential of MAs [23–32]. For instance, the authors in [23] considered a single-input-single-output (SISO) system where the transmitter and receiver were equipped with a single MA, respectively, and modelled the channel of this MA system. They found that the signal-to-noise ratio (SNR) performance can be significantly improved using MAs. Ref. [24] proposed deploying multiple MAs at the transmitter and receiver to boost the system's achievable rate. It has been demonstrated in [24] that the achievable rate can be remarkably increased by optimizing the positions of the MAs. In [25], an uplink multiuser single-input-multiple-output system, where each user is equipped with a single MA and the BS exploits a conventional uniform planar array (UPA), was proposed. By appropriately adjusting the MAs' positions, the total transmit power of all users was dramatically reduced. The authors in [26] designed a multibeam forming scheme by leveraging a linear MA array. By solving a max-min beamforming gain optimization problem, the beamforming gain of the desired directions was enhanced, whereas that of the interference directions was suppressed. Ref. [27] accounted for a wideband SISO system, with the transmitter and receiver each equipped with a single MA. It has been shown in [27] that deploying MAs can drastically improve the achievable rate through both theoretical analysis and optimization. In [28], MAs were adopted in satellite communication to significantly extend the dynamic beam coverage. The authors in [29] considered NF communication in which MAs are partitioned into multiple subarrays, with each subarray moving flexibly. The minimal achievable rate increased remarkably upon deployment of the MA array. Ref. [30] investigated a multicast communication system enabled by MAs and demonstrated that the minimal SNR in a single-group scenario and the minimal signal-to-interference-plus-noise ratio in a multigroup scenario were significantly improved. In [31], a two-timescale transmission strategy for an MA-enabled communication system was developed. On the

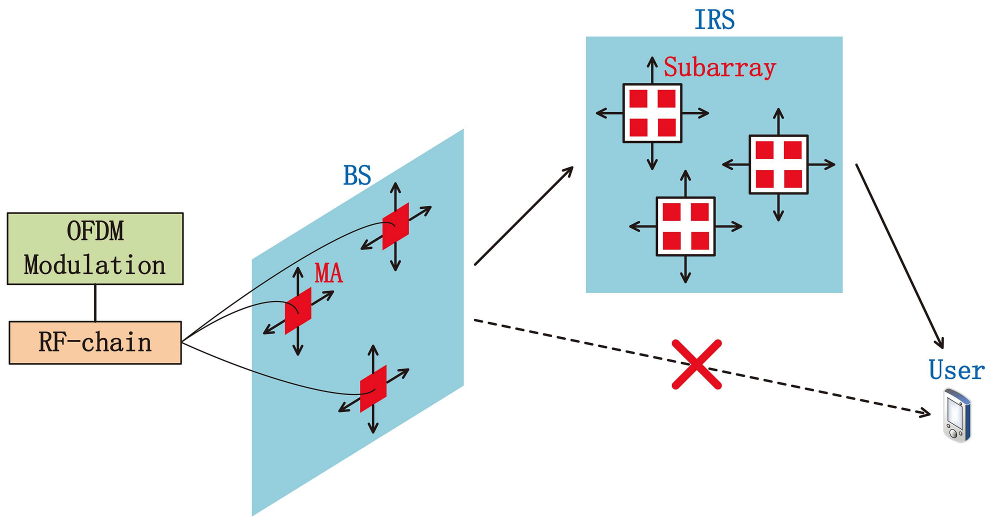

Figure 1 (Color online) Wideband MISO MA-enabled communication system aided by an IRS with movable subarrays.

large timescale, the configuration of MAs was optimized based on statistical CSI, whereas on the small timescale, instantaneous CSI was used to design the BS beamforming. This scheme drastically lowered the operational complexity and boosted the ergodic sum-rate. Meanwhile, the authors in [32] proposed deploying an MA array in a wideband communication system to mitigate the severe beam squint effect. They found that the beam squint effect can be eliminated by optimizing the positions of MAs. Motivated by the above advantages, previous studies have considered introducing MAs into THz communication systems, e.g., [33, 34], thereby demonstrating that the minimal beam gain and minimal SNR can be improved with carefully designed MA configurations.

1.2 Motivations

Given the complementary advantages of IRS and MA, communication systems integrating both technologies have been proposed recently in [35–39]. For instance, Ref. [35] considered improving the sum-rate by utilizing an IRS in the communication system, where the BS is equipped with an MA array. In [36], both IRS and MA arrays were deployed in an ISAC system to enhance the minimal beampattern gain at target sensing angles. The authors in [37] proposed an IRS-ISAC system assisted by MAs to enhance secure information transmission and accurate sensing. Notably, the IRS architecture adopted in these previous studies [35–37] was conventionally fixed; that is, the IRS elements cannot move. In contrast, movable IRS elements provide additional degrees of freedom (DoFs), which can improve the performance of wireless communication, e.g., [38, 39]. Specifically, Ref. [38] accounted for the nonuniform discrete phase shifts of IRS elements and exploited movable IRS elements to overcome the phase distribution offset, thereby improving the rate. In [39], a communication system incorporating a BS equipped with an MA array and an IRS employing movable elements was designed to boost its sum-rate. However, wideband communication systems with both IRS and MA have not been thoroughly investigated. Moreover, in the THz frequency band, due to the large IRS required to provide sufficient beamforming gain, element-wise movement results in high power consumption and increased hardware cost.

For IRS-assisted wideband systems, one prominent challenge is the double beam squint effect [40], which arises from the multiplicative nature of the analog beamforming gains at the BS and the IRS. Specifically, when the subcarrier frequency significantly differs from the reference tone (e.g., central frequency), the analog beamforming gains at the BS and at the IRS severely degrade, further undermining the array gain of the BS-IRS-user link. As reported in [32], the beam squint effect can be remarkably alleviated by deploying an MA array in the wideband communication system. Inspired by the above observations, we are motivated to investigate the implementation of movable elements at both the BS and the IRS to effectively mitigate the double beam squint effect in THz wideband systems. To maintain the low complexity and hardware cost at the IRS, the reflecting elements are grouped into multiple subarrays, each of which can flexibly move within the IRS surface (Figure 1).

1.3 Contributions

In this paper, we investigate mitigating the double beam squint effect in IRS-aided THz wideband communication. The contributions of this paper are summarized as follows.

• First, as shown in Figure 1, because the double beam squint effect is caused by the beam squint occurring at both the BS and IRS, we propose the deployment of an MA array at the BS and the use of movable elements embedded in the IRS to suppress the beam squint effect at the BS and IRS sides to mitigate the double beam squint effect. Because of the high costs of element-wise movement at the IRS, we partition the IRS elements into multiple subarrays, with each subarray moving freely. To the best of the authors' knowledge, existing studies have not yet considered the double beam squint effect suppression scheme in wideband THz communication systems with MA array deployment at the BS and the utilization of movable IRS subarrays [23–39].

• Second, to mitigate the double beam squint effect, we propose a max-min criterion to jointly configure the MAs' and IRS subarrays' positions, thereby maximizing the minimum received power over a wide THz frequency band. Our formulated optimization problem is nonconvex because of the max-min form of the objective and nonconvex constraints guaranteeing the avoidance of antenna coupling and subarray collision, making it difficult to solve. Although existing studies have studied max-min beamforming gain problems [26, 32, 33, 36], they either did not account for wideband communications [26, 33, 36] or did not consider IRS employment [26, 32, 33]. To the best of the authors' knowledge, this is the first work to investigate the joint configuration of movable components within the BS and the IRS to alleviate the double beam squint effect.

• Furthermore, to solve the above challenging optimization problem, we develop an algorithm based on the appropriate transformation and the majorization-minimization (MM) [41] framework. Specifically, the complex objective can be equivalently reformulated as constraints by introducing a slack variable. Then, we use the block coordinate descent (BCD) [42] method to obtain a more tractable solution, where all nonconvex constraints are handled using the MM methodology. Notably, the designed algorithm can yield monotonically increasing objective values that converge according to theoretical analysis.

• Lastly, numerical results illustrate the effectiveness of our proposed algorithm and demonstrate the benefits of exploiting movable elements at the BS and IRS for mitigating the double beam squint effect in IRS-aided wideband THz communication. In particular, our proposed solution can eliminate the double beam squint effect by delicately adjusting all movable components. Besides, appropriately enlarging the IRS subarray results in only slight performance degradation compared with element-wise movement, while significantly reducing hardware costs and computational complexity.

The rest of this paper is organized as follows. Section 2 introduces the system model, the double beam squint effect, and the problem formulation. Section 3 develops the proposed algorithm to address the nonconvex max-min received power problem. Simulation results are presented in Section 4 to verify the effectiveness of the proposed algorithm and the strategy for suppressing the double beam squint effect. Section 5 presents the conclusion of this paper.

Notations. x, $\mathbf{x}$, and $\mathbf{X}$ denote scalars, vectors, and matrices, respectively. $\mathbf{X}^{\mathsf{T}}$, $\mathbf{X}^{\mathsf{H}}$, and $\mathbf{X}^*$ denote the transpose, conjugate transpose, and conjugate of $\mathbf{X}$, respectively. $\mathbf{X} \succeq \mathbf{Y}$ ($\mathbf{X} \preceq \mathbf{Y}$) indicates that $\mathbf{X} - \mathbf{Y}$ is positive (negative) semidefinite. $\mathbf{I}_n$ denotes the identity matrix of size $n \times n$. $\odot$ denotes the Hadamard product. $|\cdot|$ and $\|\cdot\|_2$ denote the modulus and 2-norm, respectively. $\mathsf{Diag}(\cdot)$ denotes the diagonal of a vector. $\mathbb{E}\{\cdot\}$ denotes the expectation operation. $\angle(\cdot)$ denotes taking the phase of the input scalar.

2 System model and problem formulation

2.1 System model

As shown in Figure 1, we consider an IRS-aided wideband THz multiple-input-single-output (MISO) communication system, where a multi-antenna BS serves a single-antenna user with the assistance of an IRS. The BS is equipped with a two-dimensional planar array of size $A_{\mathrm{BS},1} \times A_{\mathrm{BS},2}$, which includes M MAs, and the IRS is shaped as a two-dimensional planar surface of size $A_{\mathrm{IRS},1} \times A_{\mathrm{IRS},2}$. Use $\mathcal{M} \triangleq \{1, \dots, M\}$ to denote the set of MAs and $\mathbf{p}_m^{\mathrm{B}}$, $m \in \mathcal{M}$, to denote the relative position of the m-th MA with respect to (w.r.t.) the center of the BS array. Since all MAs should not move out of the BS array, each should guarantee $\mathbf{p}_m^{\mathrm{B}} \in \mathcal{C}_{\mathrm{BS}} \triangleq \{(x, y) | x \in [-\frac{A_{\mathrm{BS},1}}{2}, \frac{A_{\mathrm{BS},1}}{2}],\ y \in [-\frac{A_{\mathrm{BS},2}}{2}, \frac{A_{\mathrm{BS},2}}{2}]\}$, $m \in \mathcal{M}$, where $\mathcal{C}_{\mathrm{BS}}$ represents the feasible moving region of the MAs.

The IRS elements are partitioned into K subarrays, each of which can move flexibly on the IRS surface. Each subarray has the shape of UPA consisting of $J = J_1 J_2$ reflecting elements, where J_1 and J_2 stand for the number of reflecting elements along its horizontal and vertical directions, respectively. Hence, the IRS has $N = KJ$ reflecting elements in total. Use $\mathcal{K} \triangleq \{1, \dots, K\}$ and $\mathcal{J} \triangleq \{1, \dots, J\}$ to denote the sets of IRS subarrays and reflecting elements within one subarray, respectively. Furthermore, we define $\mathbf{c}_k^{\mathrm{R}}$, $k \in \mathcal{K}$, as the relative position of the k-th subarray's center w.r.t. the center of the IRS surface and $\mathbf{t}_{k,j}^{\mathrm{R}}$, $k \in \mathcal{K}$, $j \in \mathcal{J}$, as the relative position of the j-th reflecting element w.r.t. the center of the k-th subarray. Since all reflecting elements should maintain within the IRS surface, the constraint $\mathbf{c}_k^{\mathrm{R}} + \mathbf{t}_{k,j}^{\mathrm{R}} \in \mathcal{C}_{\mathrm{IRS}} \triangleq \{(x,y)|x \in [-\frac{A_{\mathrm{IRS},1}}{2}, \frac{A_{\mathrm{IRS},1}}{2}],\ y \in [-\frac{A_{\mathrm{IRS},2}}{2}, \frac{A_{\mathrm{IRS},2}}{2}]\},\ k \in \mathcal{K},\ j \in \mathcal{J}$, should be satisfied, where $\mathcal{C}_{\mathrm{IRS}}$ represents the feasible dwelling region of the reflecting elements.

In this paper, we consider the quasi-static far-field channel model. Since the attenuation of the THz channel is severe, we assume that all channels only include line-of-sight (LoS) components. Besides, without loss of generality, the direct link between the BS and the user is severely blocked. Use $f_l, l \in \mathcal{L} \triangleq \{0, \ldots, L\}$ to denote the frequency of the l-th subcarrier with $f_0 < \cdots < f_L$. Then, the channel between the BS and IRS at the l-th subcarrier is given by

$$\mathbf{G}_l(\tilde{\mathbf{p}}_{\mathrm{B}}, \tilde{\mathbf{c}}_{\mathrm{R}}) = \alpha_{\mathrm{G},l} \mathrm{e}^{-\mathrm{j}2\pi\tau_{\mathrm{G}} f_l} \mathbf{a}(\tilde{\mathbf{c}}_{\mathrm{R}}, f_l, \vartheta_{\mathrm{R}}^{\mathrm{r}}, \varphi_{\mathrm{R}}^{\mathrm{r}}) \mathbf{b}^{\mathsf{H}}(\tilde{\mathbf{p}}_{\mathrm{B}}, f_l, \vartheta_{\mathrm{B}}, \varphi_{\mathrm{B}}),\ l \in \mathcal{L}, \tag{1}$$

where $\tilde{\mathbf{p}}_{\mathrm{B}} \triangleq [(\mathbf{p}_1^{\mathrm{B}})^{\mathsf{T}}, \ldots, (\mathbf{p}_M^{\mathrm{B}})^{\mathsf{T}}]^{\mathsf{T}}$ and $\tilde{\mathbf{c}}_{\mathrm{R}} \triangleq [(\mathbf{c}_1^{\mathrm{R}})^{\mathsf{T}}, \ldots, (\mathbf{c}_K^{\mathrm{R}})^{\mathsf{T}}]^{\mathsf{T}}$ represent the position vectors of MAs and IRS subarrays, respectively. τ_{G} stands for the path delay of the BS-IRS channel. $\alpha_{\mathrm{G},l}$ represents the path loss of the BS-IRS channel at the l-th subcarrier, which can be expressed as

$$\alpha_{\mathrm{G},l} = \frac{c}{4\pi f_l d_{\mathrm{G}}} \mathrm{e}^{-\frac{1}{2}\kappa_{\mathrm{abs}}(f_l) d_{\mathrm{G}}}, \tag{2}$$

where c, d_{G}, and $\kappa_{\mathrm{abs}}(f_l)$ are the speed of light, the distance between the BS and IRS, and the molecular absorption factor, respectively. $\mathbf{a}(\tilde{\mathbf{c}}_{\mathrm{R}}, f_l, \vartheta_{\mathrm{R}}^{\mathrm{r}}, \varphi_{\mathrm{R}}^{\mathrm{r}})$ indicates the steering vector at the IRS, which is given by

$$\mathbf{a}(\tilde{\mathbf{c}}_{\mathrm{R}}, f_l, \vartheta_{\mathrm{R}}^{\mathrm{r}}, \varphi_{\mathrm{R}}^{\mathrm{r}}) = [\mathbf{a}_1^{\mathsf{T}}(\mathbf{c}_1^{\mathrm{R}}, f_l, \vartheta_{\mathrm{R}}^{\mathrm{r}}, \varphi_{\mathrm{R}}^{\mathrm{r}}), \ldots, \mathbf{a}_K^{\mathsf{T}}(\mathbf{c}_K^{\mathrm{R}}, f_l, \vartheta_{\mathrm{R}}^{\mathrm{r}}, \varphi_{\mathrm{R}}^{\mathrm{r}})]^{\mathsf{T}}, \tag{3}$$

where $\mathbf{a}_k(\mathbf{c}_k^{\mathrm{R}}, f_l, \vartheta_{\mathrm{R}}^{\mathrm{r}}, \varphi_{\mathrm{R}}^{\mathrm{r}}),\ k \in \mathcal{K}$, represents the steering vector at the k-th IRS subarray, which reads

$$\mathbf{a}_k(\mathbf{c}_k^{\mathrm{R}}, f_l, \vartheta_{\mathrm{R}}^{\mathrm{r}}, \varphi_{\mathrm{R}}^{\mathrm{r}}) = \left[\mathrm{e}^{\mathrm{j}\frac{2\pi f_l}{c}(\mathbf{c}_k^{\mathrm{R}} + \mathbf{t}_{k,1}^{\mathrm{R}})^{\mathsf{T}} \boldsymbol{\rho}_{\mathrm{R}}^{\mathrm{r}}}, \ldots, \mathrm{e}^{\mathrm{j}\frac{2\pi f_l}{c}(\mathbf{c}_k^{\mathrm{R}} + \mathbf{t}_{k,J}^{\mathrm{R}})^{\mathsf{T}} \boldsymbol{\rho}_{\mathrm{R}}^{\mathrm{r}}}\right]^{\mathsf{T}}, \tag{4}$$

where $\boldsymbol{\rho}_{\mathrm{R}}^{\mathrm{r}} \triangleq [\sin\vartheta_{\mathrm{R}}^{\mathrm{r}} \sin\varphi_{\mathrm{R}}^{\mathrm{r}}, \cos\varphi_{\mathrm{R}}^{\mathrm{r}}]^{\mathsf{T}}$, with $\vartheta_{\mathrm{R}}^{\mathrm{r}}$ and $\varphi_{\mathrm{R}}^{\mathrm{r}}$ being the azimuth and elevation angles of angle-of-arrival (AoA) at the IRS, respectively[1)] [43–45]. $\mathbf{b}(\tilde{\mathbf{p}}_{\mathrm{B}}, f_l, \vartheta_{\mathrm{B}}, \varphi_{\mathrm{B}})$ stands for the steering vector at the BS, which can be written as

$$\mathbf{b}(\tilde{\mathbf{p}}_{\mathrm{B}}, f_l, \vartheta_{\mathrm{B}}, \varphi_{\mathrm{B}}) = \left[\mathrm{e}^{\mathrm{j}\frac{2\pi f_l}{c}(\mathbf{p}_1^{\mathrm{B}})^{\mathsf{T}} \boldsymbol{\rho}_{\mathrm{B}}}, \ldots, \mathrm{e}^{\mathrm{j}\frac{2\pi f_l}{c}(\mathbf{p}_M^{\mathrm{B}})^{\mathsf{T}} \boldsymbol{\rho}_{\mathrm{B}}}\right]^{\mathsf{T}}, \tag{5}$$

where $\boldsymbol{\rho}_{\mathrm{B}} \triangleq [\cos\vartheta_{\mathrm{B}} \sin\varphi_{\mathrm{B}}, \cos\varphi_{\mathrm{B}}]^{\mathsf{T}}$, with ϑ_{B} and φ_{B} being the azimuth and elevation angles of angle-of-departure (AoD) at the BS, respectively.

Similarly, the channel between the IRS and the user at the l-th subcarrier is given as follows:

$$\mathbf{h}_l(\tilde{\mathbf{c}}_{\mathrm{R}}) = \alpha_{\mathrm{h},l} \mathrm{e}^{-\mathrm{j}2\pi\tau_{\mathrm{h}} f_l} \mathbf{a}(\tilde{\mathbf{c}}_{\mathrm{R}}, f_l, \vartheta_{\mathrm{R}}^{\mathrm{t}}, \varphi_{\mathrm{R}}^{\mathrm{t}}),\ l \in \mathcal{L}, \tag{6}$$

where τ_{h} represents the path delay of the IRS-user channel. $\vartheta_{\mathrm{R}}^{\mathrm{t}}$ and $\varphi_{\mathrm{R}}^{\mathrm{t}}$ are the azimuth and elevation angles of AoD at the IRS, respectively. $\alpha_{\mathrm{h},l}$ indicates the path loss of the IRS-user channel at the l-th subcarrier, which can be expressed as

$$\alpha_{\mathrm{h},l} = \frac{c}{4\pi f_l d_{\mathrm{h}}} \mathrm{e}^{-\frac{1}{2}\kappa_{\mathrm{abs}}(f_l) d_{\mathrm{h}}}, \tag{7}$$

where d_{h} stands for the distance between the IRS and user.

The received signal of the user at the l-th subcarrier is given by

$$y_l = \mathbf{h}_l^{\mathsf{H}}(\tilde{\mathbf{c}}_{\mathrm{R}}) \boldsymbol{\Theta} \mathbf{G}_l(\tilde{\mathbf{p}}_{\mathrm{B}}, \tilde{\mathbf{c}}_{\mathrm{R}}) \mathbf{f} s_l + n_l,\ l \in \mathcal{L}, \tag{8}$$

where s_l and n_l are the transmitted signal at the BS and the thermal noise at the user, respectively, with $\mathbb{E}\{s_l\} = 0$ and $\mathbb{E}\{|s_l|^2\} = 1$, $\mathbf{f}$ and $\boldsymbol{\Theta}$ represent the BS beamforming vector and IRS phase shift matrix, respectively. For simplicity, we assume that s_l and n_l, for all $l \in \mathcal{L}$, are uncorrelated [4–6].

According to (8), the amplitude of the user's received signal at the l-th subcarrier reads[2)]

$$\mathrm{g}_l(\tilde{\mathbf{p}}_{\mathrm{B}}, \tilde{\mathbf{c}}_{\mathrm{R}}) = |\mathbf{h}_l^{\mathsf{H}}(\tilde{\mathbf{c}}_{\mathrm{R}}) \boldsymbol{\Theta} \mathbf{G}_l(\tilde{\mathbf{p}}_{\mathrm{B}}, \tilde{\mathbf{c}}_{\mathrm{R}}) \mathbf{f}|,\ l \in \mathcal{L}. \tag{9}$$

1) Note in this paper, all the mentioned azimuth and elevation angles are assumed to be known, which can be estimated by various existing sensing techniques, e.g., [43–45].

2) Note in the following, the amplitude and power of received signals do not include thermal noise.

2.2 Double beam squint effect

To investigate the impact of wide spectrum on the amplitude of the user's received signal shown by (9), we adopt the beamformers based on central frequency $f_{\rm c}$ at the BS and IRS [46], which are respectively given by

$$\mathbf{f}(\tilde{\mathbf{p}}_{\rm B}) = \mathbf{b}(\tilde{\mathbf{p}}_{\rm B}, f_{\rm c}, \vartheta_{\rm B}, \varphi_{\rm B}), \tag{10}$$

$$\boldsymbol{\Theta}(\tilde{\mathbf{c}}_{\rm R}) = \mathsf{Diag}(\mathbf{a}(\tilde{\mathbf{c}}_{\rm R}, f_{\rm c}, \vartheta_{\rm R}^{\rm t}, \varphi_{\rm R}^{\rm t}) \odot \mathbf{a}^*(\tilde{\mathbf{c}}_{\rm R}, f_{\rm c}, \vartheta_{\rm R}^{\rm r}, \varphi_{\rm R}^{\rm r})). \tag{11}$$

Besides, based on (9), $\mathsf{g}_l(\tilde{\mathbf{p}}_{\rm B}, \tilde{\mathbf{c}}_{\rm R}),\ l \in \mathcal{L}$, can be further casted as

$$\begin{aligned}\mathsf{g}_l(\tilde{\mathbf{p}}_{\rm B}, \tilde{\mathbf{c}}_{\rm R}) &= \alpha_{{\rm G},l}\alpha_{{\rm h},l} |\mathbf{a}^{\mathsf{H}}(\tilde{\mathbf{c}}_{\rm R}, f_l, \vartheta_{\rm R}^{\rm t}, \varphi_{\rm R}^{\rm t}) \boldsymbol{\Theta}(\tilde{\mathbf{c}}_{\rm R}) \mathbf{a}(\tilde{\mathbf{c}}_{\rm R}, f_l, \vartheta_{\rm R}^{\rm r}, \varphi_{\rm R}^{\rm r})| |\mathbf{b}^{\mathsf{H}}(\tilde{\mathbf{p}}_{\rm B}, f_l, \vartheta_{\rm B}, \varphi_{\rm B}) \mathbf{f}(\tilde{\mathbf{p}}_{\rm B})| \\ &= \alpha_{{\rm G},l}\alpha_{{\rm h},l} \mathsf{g}_l^{\rm R}(\tilde{\mathbf{c}}_{\rm R}) \mathsf{g}_l^{\rm B}(\tilde{\mathbf{p}}_{\rm B}),\end{aligned} \tag{12}$$

where $\mathsf{g}_l^{\rm R}(\tilde{\mathbf{c}}_{\rm R}) \triangleq |\mathbf{a}^{\mathsf{H}}(\tilde{\mathbf{c}}_{\rm R}, f_l, \vartheta_{\rm R}^{\rm t}, \varphi_{\rm R}^{\rm t}) \boldsymbol{\Theta}(\tilde{\mathbf{c}}_{\rm R}) \mathbf{a}(\tilde{\mathbf{c}}_{\rm R}, f_l, \vartheta_{\rm R}^{\rm r}, \varphi_{\rm R}^{\rm r})|$ and $\mathsf{g}_l^{\rm B}(\tilde{\mathbf{p}}_{\rm B}) \triangleq |\mathbf{b}^{\mathsf{H}}(\tilde{\mathbf{p}}_{\rm B}, f_l, \vartheta_{\rm B}, \varphi_{\rm B}) \mathbf{f}(\tilde{\mathbf{p}}_{\rm B})|$. Note that $\mathsf{g}_l^{\rm R}(\tilde{\mathbf{c}}_{\rm R})$ and $\mathsf{g}_l^{\rm B}(\tilde{\mathbf{p}}_{\rm B})$ are actually the array gains of the IRS and the BS, respectively.

As indicated by (12), the amplitude of the user's received signal is related to the subcarrier frequency f_l. For the narrowband system, since the difference between f_l and $f_{\rm c}$ for all l's is sufficiently small, i.e., $f_l \approx f_{\rm c},\ \forall l \in \mathcal{L}$, the array gain of the IRS $\mathsf{g}_l^{\rm R}(\tilde{\mathbf{c}}_{\rm R})$ and that of the BS $\mathsf{g}_l^{\rm B}(\tilde{\mathbf{p}}_{\rm B})$ among all subcarriers only experience very little loss, which can be ignored. However, for the wideband system, f_l significantly deviates from $f_{\rm c}$ for lots of l's, which leads to the array gains of the IRS and the BS severely fluctuating across subcarriers. This phenomenon is the so-called beam squint effect at the IRS and the BS. Besides, due to the multiplicative nature of $\mathsf{g}_l^{\rm R}(\tilde{\mathbf{c}}_{\rm R})$ and $\mathsf{g}_l^{\rm B}(\tilde{\mathbf{p}}_{\rm B})$ according to (12), the amplitude of the user's received signal $\mathsf{g}_l(\tilde{\mathbf{p}}_{\rm B}, \tilde{\mathbf{c}}_{\rm R})$ further suffers from more severe degradation across subcarriers, which is the so-called double beam squint effect [40, 46].

2.3 Problem formulation

To alleviate the aforementioned double beam squint effect and balance the communication rate of the data stream among different subcarriers, in this paper, we propose to maximize the minimum received power among the entire frequency band by jointly configuring the MAs within the BS and the subarrays within the IRS, whose optimization problem is formulated as

$$(\mathcal{P}1): \max_{\tilde{\mathbf{p}}_{\rm B}, \tilde{\mathbf{c}}_{\rm R}} \min_{l \in \mathcal{L}}\ \mathsf{h}_l(\tilde{\mathbf{p}}_{\rm B}, \tilde{\mathbf{c}}_{\rm R}) \tag{13}$$

$$\text{s.t. } \mathbf{p}_m^{\rm B} \in \mathcal{C}_{\rm BS},\ m \in \mathcal{M}, \tag{13a}$$

$$\|\mathbf{p}_m^{\rm B} - \mathbf{p}_s^{\rm B}\|_2 \geqslant D_{\rm BS},\ m, s \in \mathcal{M},\ m \neq s, \tag{13b}$$

$$\mathbf{c}_k^{\rm R} + \mathbf{t}_{k,j}^{\rm R} \in \mathcal{C}_{\rm IRS},\ k \in \mathcal{K},\ j \in \mathcal{J}, \tag{13c}$$

$$\|\mathbf{c}_k^{\rm R} - \mathbf{c}_i^{\rm R}\|_2 \geqslant D_{\rm IRS},\ k, i \in \mathcal{K},\ k \neq i, \tag{13d}$$

where $\mathsf{h}_l(\tilde{\mathbf{p}}_{\rm B}, \tilde{\mathbf{c}}_{\rm R}) \triangleq \mathsf{g}_l^2(\tilde{\mathbf{p}}_{\rm B}, \tilde{\mathbf{c}}_{\rm R})$, constraints (13a) and (13c) indicate that each MA at the BS and each subarray at the IRS should move within the feasible region $\mathcal{C}_{\rm BS}$ and $\mathcal{C}_{\rm IRS}$, i.e., the BS antenna array and the IRS surface, respectively. Constraints (13b) and (13d) describe that each MA at the BS and each subarray at the IRS should maintain a distance of at least $D_{\rm BS}$ and $D_{\rm IRS}$ from other MAs/subarrays while moving to avoid antenna coupling and subarray collision, respectively. Problem ($\mathcal{P}1$) is highly nonconvex due to its objective and constraints (13b) and (13d), which are challenging to solve. In the following, we develop an algorithm to attack ($\mathcal{P}1$).

3 Proposed algorithm

In this section, we propose an algorithm to tackle ($\mathcal{P}1$). First, by introducing a slack variable, ($\mathcal{P}1$) can be equivalently transformed into the following more tractable form:

$$(\mathcal{P}2): \max_{\tilde{\mathbf{p}}_{\rm B}, \tilde{\mathbf{c}}_{\rm R}, \kappa}\ \kappa \tag{14}$$

$$\text{s.t. } \mathsf{h}_l(\tilde{\mathbf{p}}_{\rm B}, \tilde{\mathbf{c}}_{\rm R}) \geqslant \kappa,\ l \in \mathcal{L}, \tag{14a}$$

$$\mathbf{p}_m^{\rm B} \in \mathcal{C}_{\rm BS},\ m \in \mathcal{M}, \tag{14b}$$

$$\|\mathbf{p}_m^{\rm B} - \mathbf{p}_s^{\rm B}\|_2 \geqslant D_{\rm BS},\ m, s \in \mathcal{M},\ m \neq s, \tag{14c}$$

$$\mathbf{c}_k^{\mathrm{R}} + \mathbf{t}_{k,j}^{\mathrm{R}} \in \mathcal{C}_{\mathrm{IRS}},\ k \in \mathcal{K},\ j \in \mathcal{J}, \tag{14d}$$
$$\|\mathbf{c}_k^{\mathrm{R}} - \mathbf{c}_i^{\mathrm{R}}\|_2 \geqslant D_{\mathrm{IRS}},\ k, i \in \mathcal{K},\ k \neq i. \tag{14e}$$

In the following, we utilize the BCD [42] method to handle $(\mathcal{P}2)$ by alternatively optimizing one MA's or subarray's position at a time while keeping others fixed. Specifically, taking the antenna position of each MA at the BS into account first, the optimization w.r.t. the m-th MA's position $\mathbf{p}_m^{\mathrm{B}}$ is given by

$$(\mathcal{P}3_m) : \max_{\mathbf{p}_m^{\mathrm{B}}, \kappa} \kappa \tag{15}$$
$$\text{s.t. } \mathsf{h}_l(\mathbf{p}_m^{\mathrm{B}}) \geqslant \kappa,\ l \in \mathcal{L}, \tag{15a}$$
$$\mathbf{p}_m^{\mathrm{B}} \in \mathcal{C}_{\mathrm{BS}}, \tag{15b}$$
$$\|\mathbf{p}_m^{\mathrm{B}} - \mathbf{p}_s^{\mathrm{B}}\|_2 \geqslant D_{\mathrm{BS}},\ s \in \mathcal{M},\ m \neq s, \tag{15c}$$

which is still difficult to solve since constraints (15a) and (15c) are nonconvex. To overcome this difficulty, we exploit the MM [41] method to convexify (15a) and (15c), respectively.

Specifically, considering (15a) first, due to the fact that $\mathsf{h}_l(\mathbf{p}_m^{\mathrm{B}})$ is neither convex nor concave w.r.t. $\mathbf{p}_m^{\mathrm{B}}$, we examine its second-order Taylor expansion and replace the Hessian matrix by a smaller one to construct a tight globally lower-bound surrogate for $\mathsf{h}_l(\mathbf{p}_m^{\mathrm{B}})$. The second-order Taylor expansion of $\mathsf{h}_l(\mathbf{p}_m^{\mathrm{B}})$ w.r.t. $\mathbf{p}_m^{\mathrm{B}}$ at the point $(\mathbf{p}_m^{\mathrm{B}})^{(n)}$ is given as follows:

$$\begin{aligned}\mathsf{h}_l(\mathbf{p}_m^{\mathrm{B}}) \approx & \mathsf{h}_l((\mathbf{p}_m^{\mathrm{B}})^{(n)}) + \nabla^{\mathsf{T}}_{\mathbf{p}_m^{\mathrm{B}}} \mathsf{h}_l(\mathbf{p}_m^{\mathrm{B}})|_{\mathbf{p}_m^{\mathrm{B}} = (\mathbf{p}_m^{\mathrm{B}})^{(n)}} (\mathbf{p}_m^{\mathrm{B}} - (\mathbf{p}_m^{\mathrm{B}})^{(n)}) \\ & + (\mathbf{p}_m^{\mathrm{B}} - (\mathbf{p}_m^{\mathrm{B}})^{(n)})^{\mathsf{T}} \frac{\nabla^2_{\mathbf{p}_m^{\mathrm{B}}} \mathsf{h}_l(\mathbf{p}_m^{\mathrm{B}})|_{\mathbf{p}_m^{\mathrm{B}} = (\mathbf{p}_m^{\mathrm{B}})^{(n)}}}{2} (\mathbf{p}_m^{\mathrm{B}} - (\mathbf{p}_m^{\mathrm{B}})^{(n)}),\end{aligned} \tag{16}$$

where $\nabla_{\mathbf{p}_m^{\mathrm{B}}} \mathsf{h}_l(\mathbf{p}_m^{\mathrm{B}})$ and $\nabla^2_{\mathbf{p}_m^{\mathrm{B}}} \mathsf{h}_l(\mathbf{p}_m^{\mathrm{B}})$ are denoted as the gradient and the Hessian matrix of $\mathsf{h}_l(\mathbf{p}_m^{\mathrm{B}})$ w.r.t. $\mathbf{p}_m^{\mathrm{B}}$, respectively. Note that $\mathsf{h}_l(\mathbf{p}_m^{\mathrm{B}})$ can be recast as

$$\mathsf{h}_l(\mathbf{p}_m^{\mathrm{B}}) = \beta_l^{\mathrm{B}}(2|C_{m,l}^{\mathrm{B}}|\mathsf{cos}(F_l(\mathbf{p}_m^{\mathrm{B}})^{\mathsf{T}}\boldsymbol{\rho}_{\mathrm{B}} - \angle(C_{m,l}^{\mathrm{B}})) + |C_{m,l}^{\mathrm{B}}|^2 + 1), \tag{17}$$

where $\beta_l^{\mathrm{B}} \triangleq \alpha_{\mathrm{G},l}^2 \alpha_{\mathrm{h},l}^2 (\mathsf{g}_l^{\mathrm{R}}(\tilde{\mathbf{c}}_{\mathrm{R}}))^2$, $C_{m,l}^{\mathrm{B}} \triangleq \sum_{n=1,n\neq m}^{M} \mathrm{e}^{\mathrm{j}F_l(\mathbf{p}_n^{\mathrm{B}})^{\mathsf{T}}\boldsymbol{\rho}_{\mathrm{B}}}$, and $F_l \triangleq \frac{2\pi(f_{\mathrm{c}} - f_l)}{c}$. Then, the gradient $\nabla_{\mathbf{p}_m^{\mathrm{B}}} \mathsf{h}_l(\mathbf{p}_m^{\mathrm{B}})$ and the Hessian matrix $\nabla^2_{\mathbf{p}_m^{\mathrm{B}}} \mathsf{h}_l(\mathbf{p}_m^{\mathrm{B}})$ can be respectively given by

$$\nabla_{\mathbf{p}_m^{\mathrm{B}}} \mathsf{h}_l(\mathbf{p}_m^{\mathrm{B}}) = \left[\frac{\partial \mathsf{h}_l(\mathbf{p}_m^{\mathrm{B}})}{\partial [\mathbf{p}_m^{\mathrm{B}}]_1}, \frac{\partial \mathsf{h}_l(\mathbf{p}_m^{\mathrm{B}})}{\partial [\mathbf{p}_m^{\mathrm{B}}]_2}\right]^{\mathsf{T}}, \tag{18}$$

$$\nabla^2_{\mathbf{p}_m^{\mathrm{B}}} \mathsf{h}_l(\mathbf{p}_m^{\mathrm{B}}) = \begin{bmatrix} \frac{\partial^2 \mathsf{h}_l(\mathbf{p}_m^{\mathrm{B}})}{\partial [\mathbf{p}_m^{\mathrm{B}}]_1^2} & \frac{\partial^2 \mathsf{h}_l(\mathbf{p}_m^{\mathrm{B}})}{\partial [\mathbf{p}_m^{\mathrm{B}}]_1 \partial [\mathbf{p}_m^{\mathrm{B}}]_2} \\ \frac{\partial^2 \mathsf{h}_l(\mathbf{p}_m^{\mathrm{B}})}{\partial [\mathbf{p}_m^{\mathrm{B}}]_2 \partial [\mathbf{p}_m^{\mathrm{B}}]_1} & \frac{\partial^2 \mathsf{h}_l(\mathbf{p}_m^{\mathrm{B}})}{\partial [\mathbf{p}_m^{\mathrm{B}}]_2^2} \end{bmatrix}, \tag{19}$$

where

$$\frac{\partial \mathsf{h}_l(\mathbf{p}_m^{\mathrm{B}})}{\partial [\mathbf{p}_m^{\mathrm{B}}]_1} = -2\beta_l^{\mathrm{B}}|C_{m,l}^{\mathrm{B}}|F_l \mathsf{cos}\vartheta_{\mathrm{B}} \mathsf{sin}\varphi_{\mathrm{B}} \mathsf{sin}(F_l(\mathbf{p}_m^{\mathrm{B}})^{\mathsf{T}}\boldsymbol{\rho}_{\mathrm{B}} - \angle(C_{m,l}^{\mathrm{B}})), \tag{20}$$

$$\frac{\partial \mathsf{h}_l(\mathbf{p}_m^{\mathrm{B}})}{\partial [\mathbf{p}_m^{\mathrm{B}}]_2} = -2\beta_l^{\mathrm{B}}|C_{m,l}^{\mathrm{B}}|F_l \mathsf{cos}\varphi_{\mathrm{B}} \mathsf{sin}(F_l(\mathbf{p}_m^{\mathrm{B}})^{\mathsf{T}}\boldsymbol{\rho}_{\mathrm{B}} - \angle(C_{m,l}^{\mathrm{B}})), \tag{21}$$

$$\frac{\partial^2 \mathsf{h}_l(\mathbf{p}_m^{\mathrm{B}})}{\partial [\mathbf{p}_m^{\mathrm{B}}]_1^2} = -2\beta_l^{\mathrm{B}}|C_{m,l}^{\mathrm{B}}|(F_l \mathsf{cos}\vartheta_{\mathrm{B}} \mathsf{sin}\varphi_{\mathrm{B}})^2 \mathsf{cos}(F_l(\mathbf{p}_m^{\mathrm{B}})^{\mathsf{T}}\boldsymbol{\rho}_{\mathrm{B}} - \angle(C_{m,l}^{\mathrm{B}})), \tag{22}$$

$$\frac{\partial^2 \mathsf{h}_l(\mathbf{p}_m^{\mathrm{B}})}{\partial [\mathbf{p}_m^{\mathrm{B}}]_1 \partial [\mathbf{p}_m^{\mathrm{B}}]_2} = -2\beta_l^{\mathrm{B}}|C_{m,l}^{\mathrm{B}}|F_l^2 \mathsf{cos}\vartheta_{\mathrm{B}} \mathsf{sin}\varphi_{\mathrm{B}} \mathsf{cos}\varphi_{\mathrm{B}} \mathsf{cos}(F_l(\mathbf{p}_m^{\mathrm{B}})^{\mathsf{T}}\boldsymbol{\rho}_{\mathrm{B}} - \angle(C_{m,l}^{\mathrm{B}})), \tag{23}$$

$$\frac{\partial^2 \mathsf{h}_l(\mathbf{p}_m^{\mathrm{B}})}{\partial [\mathbf{p}_m^{\mathrm{B}}]_2 \partial [\mathbf{p}_m^{\mathrm{B}}]_1} = \frac{\partial^2 \mathsf{h}_l(\mathbf{p}_m^{\mathrm{B}})}{\partial [\mathbf{p}_m^{\mathrm{B}}]_1 \partial [\mathbf{p}_m^{\mathrm{B}}]_2}, \tag{24}$$

$$\frac{\partial^2 \mathsf{h}_l(\mathbf{p}_m^{\mathrm{B}})}{\partial [\mathbf{p}_m^{\mathrm{B}}]_2^2} = -2\beta_l^{\mathrm{B}}|C_{m,l}^{\mathrm{B}}|(F_l \mathsf{cos}\varphi_{\mathrm{B}})^2 \mathsf{cos}(F_l(\mathbf{p}_m^{\mathrm{B}})^{\mathsf{T}}\boldsymbol{\rho}_{\mathrm{B}} - \angle(C_{m,l}^{\mathrm{B}})). \tag{25}$$

Furthermore, it can be observed from (19) and (22)–(25) that the curvature of $\mathsf{h}_l(\mathbf{p}_m^{\mathrm{B}})$ is bounded, which implies that there must exist a negative semidefinite matrix $\mathbf{M}_{m,l}^{\mathrm{B}}$ such that $\mathbf{M}_{m,l}^{\mathrm{B}} \preceq \nabla^2_{\mathbf{p}_m^{\mathrm{B}}} \mathsf{h}_l(\mathbf{p}_m^{\mathrm{B}})$. In the following, we proceed to derive $\mathbf{M}_{m,l}^{\mathrm{B}}$. Specifically, let $H_{1,m,l}^{\mathrm{B}} \triangleq \frac{\partial^2 \mathsf{h}_l(\mathbf{p}_m^{\mathrm{B}})}{\partial [\mathbf{p}_m^{\mathrm{B}}]_1^2}$, $H_{2,m,l}^{\mathrm{B}} \triangleq \frac{\partial^2 \mathsf{h}_l(\mathbf{p}_m^{\mathrm{B}})}{\partial [\mathbf{p}_m^{\mathrm{B}}]_1 \partial [\mathbf{p}_m^{\mathrm{B}}]_2}$, and $H_{3,m,l}^{\mathrm{B}} \triangleq \frac{\partial^2 \mathsf{h}_l(\mathbf{p}_m^{\mathrm{B}})}{\partial [\mathbf{p}_m^{\mathrm{B}}]_2^2}$. Then, $\nabla^2_{\mathbf{p}_m^{\mathrm{B}}} \mathsf{h}_l(\mathbf{p}_m^{\mathrm{B}})$ can be rewritten as

$$\nabla^2_{\mathbf{p}_m^{\mathrm{B}}} \mathsf{h}_l(\mathbf{p}_m^{\mathrm{B}}) = \underbrace{\begin{bmatrix} H_{1,m,l}^{\mathrm{B}} & 0 \\ 0 & H_{3,m,l}^{\mathrm{B}} \end{bmatrix}}_{\triangleq \mathbf{H}_{1,m,l}^{\mathrm{B}}} + \underbrace{\begin{bmatrix} 0 & H_{2,m,l}^{\mathrm{B}} \\ H_{2,m,l}^{\mathrm{B}} & 0 \end{bmatrix}}_{\triangleq \mathbf{H}_{2,m,l}^{\mathrm{B}}}. \tag{26}$$

Therefore, the task of constructing $\mathbf{M}_{m,l}^{\mathrm{B}}$ reduces to examining the lower bounds of $\mathbf{H}_{1,m,l}^{\mathrm{B}}$ and $\mathbf{H}_{2,m,l}^{\mathrm{B}}$, respectively. Taking $\mathbf{H}_{1,m,l}^{\mathrm{B}}$ into account first, it can be observed that its lower bound can be obtained by calculating the lower bounds of $H_{1,m,l}^{\mathrm{B}}$ and $H_{3,m,l}^{\mathrm{B}}$, respectively. Since $\mathsf{cos}(\cdot) \in [-1, 1]$, according to (22) and (25), we have

$$H_{1,m,l}^{\mathrm{B}} \geqslant -2\beta_l^{\mathrm{B}} |C_{m,l}^{\mathrm{B}}| (F_l \mathsf{cos}\vartheta_{\mathrm{B}} \mathsf{sin}\varphi_{\mathrm{B}})^2, \tag{27}$$

$$H_{3,m,l}^{\mathrm{B}} \geqslant -2\beta_l^{\mathrm{B}} |C_{m,l}^{\mathrm{B}}| (F_l \mathsf{cos}\varphi_{\mathrm{B}})^2, \tag{28}$$

whose respective right hand side is indeed independent of $\mathbf{p}_m^{\mathrm{B}}$. Hence, by substituting the right hand side of (27) and that of (28) into $\mathbf{H}_{1,m,l}^{\mathrm{B}}$, a global lower bound of $\mathbf{H}_{1,m,l}^{\mathrm{B}}$ can be acquired.

Next, we derive the lower bound of $\mathbf{H}_{2,m,l}^{\mathrm{B}}$. Note that the following inequality:

$$\mathbf{H}_{2,m,l}^{\mathrm{B}} \succeq -|H_{2,m,l}^{\mathrm{B}}| \mathbf{I}_2 \tag{29}$$

naturally holds, which indicates that the lower bound of $\mathbf{H}_{2,m,l}^{\mathrm{B}}$ can be obtained by checking the upper bound of $|H_{2,m,l}^{\mathrm{B}}|$. Due to the fact that $\mathsf{cos}(\cdot) \in [-1, 1]$, $\mathbf{H}_{2,m,l}^{\mathrm{B}}$ can be upper-bounded by

$$|H_{2,m,l}^{\mathrm{B}}| \leqslant 2\beta_l^{\mathrm{B}} |C_{m,l}^{\mathrm{B}}| F_l^2 |\mathsf{cos}\vartheta_{\mathrm{B}} \mathsf{sin}\varphi_{\mathrm{B}} \mathsf{cos}\varphi_{\mathrm{B}}|. \tag{30}$$

Since the right hand side of (30) is unrelated to $\mathbf{p}_m^{\mathrm{B}}$, we can acquire a global lower bound of $\mathbf{H}_{2,m,l}^{\mathrm{B}}$ via replacing $|H_{2,m,l}^{\mathrm{B}}|$ in (29) by the right hand side of (30), and thus the derivation of $\mathbf{M}_{m,l}^{\mathrm{B}}$ is completed. Lastly, by substituting $\mathbf{M}_{m,l}^{\mathrm{B}}$ into (16), a globally concave lower bound of $\mathsf{h}_l(\mathbf{p}_m^{\mathrm{B}})$, denoted by $\mathsf{h}_l(\mathbf{p}_m^{\mathrm{B}} | (\mathbf{p}_m^{\mathrm{B}})^{(n)})$, can be obtained, which is given by

$$\begin{aligned} \mathsf{h}_l(\mathbf{p}_m^{\mathrm{B}} | (\mathbf{p}_m^{\mathrm{B}})^{(n)}) = & \mathsf{h}_l((\mathbf{p}_m^{\mathrm{B}})^{(n)}) + \nabla^{\mathsf{T}}_{\mathbf{p}_m^{\mathrm{B}}} \mathsf{h}_l(\mathbf{p}_m^{\mathrm{B}})|_{\mathbf{p}_m^{\mathrm{B}} = (\mathbf{p}_m^{\mathrm{B}})^{(n)}} (\mathbf{p}_m^{\mathrm{B}} - (\mathbf{p}_m^{\mathrm{B}})^{(n)}) \\ & + (\mathbf{p}_m^{\mathrm{B}} - (\mathbf{p}_m^{\mathrm{B}})^{(n)})^{\mathsf{T}} \frac{\mathbf{M}_{m,l}^{\mathrm{B}}}{2} (\mathbf{p}_m^{\mathrm{B}} - (\mathbf{p}_m^{\mathrm{B}})^{(n)}). \end{aligned} \tag{31}$$

In the following, we resolve the non-convexity of (15c), which is much easier because the left hand side of (15c) is convex w.r.t. $\mathbf{p}_m^{\mathrm{B}}$ such that its first-order Taylor expansion serves as a globally concave lower bound. Therefore, by leveraging the following first-order Taylor expansion:

$$\|\mathbf{p}_m^{\mathrm{B}} - \mathbf{p}_s^{\mathrm{B}}\|_2 \geqslant \frac{((\mathbf{p}_m^{\mathrm{B}})^{(n)} - \mathbf{p}_s^{\mathrm{B}})^{\mathsf{T}}}{\|(\mathbf{p}_m^{\mathrm{B}})^{(n)} - \mathbf{p}_s^{\mathrm{B}}\|_2} (\mathbf{p}_m^{\mathrm{B}} - \mathbf{p}_s^{\mathrm{B}}), \tag{32}$$

the convexification for (15c) can be achieved.

Based on the above two developed concave lower bounds (31) and (32), a convex optimization problem can be acquired, given as follows:

$$(\mathcal{P}4_m): \max_{\mathbf{p}_m^{\mathrm{B}}, \kappa} \kappa \tag{33}$$

$$\text{s.t. } \mathsf{h}_l(\mathbf{p}_m^{\mathrm{B}} | (\mathbf{p}_m^{\mathrm{B}})^{(n)}) \geqslant \kappa, \ l \in \mathcal{L}, \tag{33a}$$

$$\mathbf{p}_m^{\mathrm{B}} \in \mathcal{C}_{\mathrm{BS}}, \tag{33b}$$

$$\frac{((\mathbf{p}_m^{\mathrm{B}})^{(n)} - \mathbf{p}_s^{\mathrm{B}})^{\mathsf{T}}}{\|(\mathbf{p}_m^{\mathrm{B}})^{(n)} - \mathbf{p}_s^{\mathrm{B}}\|_2} (\mathbf{p}_m^{\mathrm{B}} - \mathbf{p}_s^{\mathrm{B}}) \geqslant D_{\mathrm{BS}}, \ s \in \mathcal{M}, \ m \neq s, \tag{33c}$$

which can be solved by the existing standard numerical solvers, e.g., CVX.

Next, we proceed to optimize the position of each IRS subarray with other variables being fixed. The subproblem w.r.t. the k-th subarray's position $\mathbf{c}_k^{\mathrm{R}}$ can be expressed as

$$(\mathcal{P}5_k): \max_{\mathbf{c}_k^{\mathrm{R}},\kappa} \kappa \tag{34}$$

$$\text{s.t. } \mathsf{h}_l(\mathbf{c}_k^{\mathrm{R}}) \geqslant \kappa,\ l\in\mathcal{L}, \tag{34a}$$

$$\mathbf{c}_k^{\mathrm{R}} + \mathbf{t}_{k,j}^{\mathrm{R}} \in \mathcal{C}_{\mathrm{IRS}},\ j\in\mathcal{J}, \tag{34b}$$

$$\|\mathbf{c}_k^{\mathrm{R}} - \mathbf{c}_i^{\mathrm{R}}\|_2 \geqslant D_{\mathrm{IRS}},\ i\in\mathcal{K},\ k\neq i, \tag{34c}$$

which is non-convex due to constraints (34a) and (34c). Taking (34a) into consideration first, similar to the procedure of convexifying (15a), we tackle (34a) via adopting the second-order Taylor expansion of $\mathsf{h}_l(\mathbf{c}_k^{\mathrm{R}})$ due to the non-convexity and non-concavity of $\mathsf{h}_l(\mathbf{c}_k^{\mathrm{R}})$, and surrogating its Hessian matrix by a smaller one which is negative semidefinite. The second-order Taylor expansion of $\mathsf{h}_l(\mathbf{c}_k^{\mathrm{R}})$ w.r.t. $\mathbf{c}_k^{\mathrm{R}}$ at the point $(\mathbf{c}_k^{\mathrm{R}})^{(n)}$ is given by

$$\begin{aligned}\mathsf{h}_l(\mathbf{c}_k^{\mathrm{R}}) \approx&\mathsf{h}_l((\mathbf{c}_k^{\mathrm{R}})^{(n)}) + \nabla^{\mathsf{T}}_{\mathbf{c}_k^{\mathrm{R}}}\mathsf{h}_l(\mathbf{c}_k^{\mathrm{R}})|_{\mathbf{c}_k^{\mathrm{R}}=(\mathbf{c}_k^{\mathrm{R}})^{(n)}}(\mathbf{c}_k^{\mathrm{R}}-(\mathbf{c}_k^{\mathrm{R}})^{(n)})\\ &+(\mathbf{c}_k^{\mathrm{R}}-(\mathbf{c}_k^{\mathrm{R}})^{(n)})^{\mathsf{T}}\frac{\nabla^2_{\mathbf{c}_k^{\mathrm{R}}}\mathsf{h}_l(\mathbf{c}_k^{\mathrm{R}})|_{\mathbf{c}_k^{\mathrm{R}}=(\mathbf{c}_k^{\mathrm{R}})^{(n)}}}{2}(\mathbf{c}_k^{\mathrm{R}}-(\mathbf{c}_k^{\mathrm{R}})^{(n)}),\end{aligned} \tag{35}$$

where $\nabla_{\mathbf{c}_k^{\mathrm{R}}}\mathsf{h}_l(\mathbf{c}_k^{\mathrm{R}})$ and $\nabla^2_{\mathbf{c}_k^{\mathrm{R}}}\mathsf{h}_l(\mathbf{c}_k^{\mathrm{R}})$ represent the gradient and the Hessian matrix of $\mathsf{h}_l(\mathbf{c}_k^{\mathrm{R}})$ w.r.t. $\mathbf{c}_k^{\mathrm{R}}$, respectively. Similar to $\mathsf{h}_l(\mathbf{p}_m^{\mathrm{B}})$, $\mathsf{h}_l(\mathbf{c}_k^{\mathrm{R}})$ can be recasted as

$$\begin{aligned}\mathsf{h}_l(\mathbf{c}_k^{\mathrm{R}}) =&\beta_l^{\mathrm{R}}\Bigg(2|C_{k,l}^{\mathrm{R}}|\sum_{j=1}^{J}\cos(F_l(\mathbf{c}_k^{\mathrm{R}}+\mathbf{t}_{k,j}^{\mathrm{R}})^{\mathsf{T}}(\boldsymbol{\rho}_{\mathrm{R}}^{\mathrm{t}}-\boldsymbol{\rho}_{\mathrm{R}}^{\mathrm{r}})-\angle(C_{k,l}^{\mathrm{R}}))\\ &+|\mathbf{a}_k^{\mathsf{H}}(\mathbf{c}_k^{\mathrm{R}},f_l,\vartheta_{\mathrm{R}}^{\mathrm{t}},\varphi_{\mathrm{R}}^{\mathrm{t}})\boldsymbol{\Theta}_k(\mathbf{c}_k^{\mathrm{R}})\mathbf{a}_k(\mathbf{c}_k^{\mathrm{R}},f_l,\vartheta_{\mathrm{R}}^{\mathrm{r}},\varphi_{\mathrm{R}}^{\mathrm{r}})|^2+|C_{k,l}^{\mathrm{R}}|^2\Bigg)\\ =&\beta_l^{\mathrm{R}}\left(2|C_{k,l}^{\mathrm{R}}|\sum_{j=1}^{J}\cos(F_l(\mathbf{c}_k^{\mathrm{R}}+\mathbf{t}_{k,j}^{\mathrm{R}})^{\mathsf{T}}(\boldsymbol{\rho}_{\mathrm{R}}^{\mathrm{t}}-\boldsymbol{\rho}_{\mathrm{R}}^{\mathrm{r}})-\angle(C_{k,l}^{\mathrm{R}}))+\left|\sum_{j=1}^{J}\mathrm{e}^{\mathrm{j}F_l(\mathbf{t}_{k,j}^{\mathrm{R}})^{\mathsf{T}}(\boldsymbol{\rho}_{\mathrm{R}}^{\mathrm{t}}-\boldsymbol{\rho}_{\mathrm{R}}^{\mathrm{r}})}\right|^2+|C_{k,l}^{\mathrm{R}}|^2\right),\end{aligned} \tag{36}$$

where $\boldsymbol{\rho}_{\mathrm{R}}^{\mathrm{t}} \triangleq [\sin\vartheta_{\mathrm{R}}^{\mathrm{t}}\sin\varphi_{\mathrm{R}}^{\mathrm{t}},\cos\varphi_{\mathrm{R}}^{\mathrm{t}}]^{\mathsf{T}}$, $\beta_l^{\mathrm{R}} \triangleq \alpha_{\mathrm{G},l}^2\alpha_{\mathrm{h},l}^2(\mathsf{g}_l^{\mathrm{B}}(\tilde{\mathbf{p}}_{\mathrm{B}}))^2$, $\boldsymbol{\Theta}_k(\mathbf{c}_k^{\mathrm{R}}) \triangleq \mathsf{Diag}(\mathbf{a}_k(\mathbf{c}_k^{\mathrm{R}},f_{\mathrm{c}},\vartheta_{\mathrm{R}}^{\mathrm{t}},\varphi_{\mathrm{R}}^{\mathrm{t}})\odot\mathbf{a}_k^*(\mathbf{c}_k^{\mathrm{R}},f_{\mathrm{c}},\vartheta_{\mathrm{R}}^{\mathrm{r}},\varphi_{\mathrm{R}}^{\mathrm{r}}))$, and $C_{k,l}^{\mathrm{R}} \triangleq \sum_{n=1,n\neq k}^{K}\mathbf{a}_n^{\mathsf{H}}(\mathbf{c}_n^{\mathrm{R}},f_l,\vartheta_{\mathrm{R}}^{\mathrm{t}},\varphi_{\mathrm{R}}^{\mathrm{t}})\boldsymbol{\Theta}_n(\mathbf{c}_n^{\mathrm{R}})\mathbf{a}_n(\mathbf{c}_n^{\mathrm{R}},f_l,\vartheta_{\mathrm{R}}^{\mathrm{r}},\varphi_{\mathrm{R}}^{\mathrm{r}})$. Meanwhile, the second equality follows the fact that $|\mathbf{a}_k^{\mathsf{H}}(\mathbf{c}_k^{\mathrm{R}},f_l,\vartheta_{\mathrm{R}}^{\mathrm{t}},\varphi_{\mathrm{R}}^{\mathrm{t}})\boldsymbol{\Theta}_k(\mathbf{c}_k^{\mathrm{R}})\mathbf{a}_k(\mathbf{c}_k^{\mathrm{R}},f_l,\vartheta_{\mathrm{R}}^{\mathrm{r}},\varphi_{\mathrm{R}}^{\mathrm{r}})| = |\sum_{j=1}^{J}\mathrm{e}^{\mathrm{j}F_l(\mathbf{c}_k^{\mathrm{R}})^{\mathsf{T}}(\boldsymbol{\rho}_{\mathrm{R}}^{\mathrm{t}}-\boldsymbol{\rho}_{\mathrm{R}}^{\mathrm{r}})}\mathrm{e}^{\mathrm{j}F_l(\mathbf{t}_{k,j}^{\mathrm{R}})^{\mathsf{T}}(\boldsymbol{\rho}_{\mathrm{R}}^{\mathrm{t}}-\boldsymbol{\rho}_{\mathrm{R}}^{\mathrm{r}})}| = |\mathrm{e}^{\mathrm{j}F_l(\mathbf{c}_k^{\mathrm{R}})^{\mathsf{T}}(\boldsymbol{\rho}_{\mathrm{R}}^{\mathrm{t}}-\boldsymbol{\rho}_{\mathrm{R}}^{\mathrm{r}})} \times \sum_{j=1}^{J}\mathrm{e}^{\mathrm{j}F_l(\mathbf{t}_{k,j}^{\mathrm{R}})^{\mathsf{T}}(\boldsymbol{\rho}_{\mathrm{R}}^{\mathrm{t}}-\boldsymbol{\rho}_{\mathrm{R}}^{\mathrm{r}})}| = |\sum_{j=1}^{J}\mathrm{e}^{\mathrm{j}F_l(\mathbf{t}_{k,j}^{\mathrm{R}})^{\mathsf{T}}(\boldsymbol{\rho}_{\mathrm{R}}^{\mathrm{t}}-\boldsymbol{\rho}_{\mathrm{R}}^{\mathrm{r}})}|$, which is independent of $\mathbf{c}_k^{\mathrm{R}}$. Then, the gradient $\nabla_{\mathbf{c}_k^{\mathrm{R}}}\mathsf{h}_l(\mathbf{c}_k^{\mathrm{R}})$ and the Hessian matrix $\nabla^2_{\mathbf{c}_k^{\mathrm{R}}}\mathsf{h}_l(\mathbf{c}_k^{\mathrm{R}})$ can be respectively written as

$$\nabla_{\mathbf{c}_k^{\mathrm{R}}}\mathsf{h}_l(\mathbf{c}_k^{\mathrm{R}}) = \left[\frac{\partial\mathsf{h}_l(\mathbf{c}_k^{\mathrm{R}})}{\partial[\mathbf{c}_k^{\mathrm{R}}]_1},\frac{\partial\mathsf{h}_l(\mathbf{c}_k^{\mathrm{R}})}{\partial[\mathbf{c}_k^{\mathrm{R}}]_2}\right]^{\mathsf{T}}, \tag{37}$$

$$\nabla^2_{\mathbf{c}_k^{\mathrm{R}}}\mathsf{h}_l(\mathbf{c}_k^{\mathrm{R}}) = \begin{bmatrix}\dfrac{\partial^2\mathsf{h}_l(\mathbf{c}_k^{\mathrm{R}})}{\partial[\mathbf{c}_k^{\mathrm{R}}]_1^2} & \dfrac{\partial^2\mathsf{h}_l(\mathbf{c}_k^{\mathrm{R}})}{\partial[\mathbf{c}_k^{\mathrm{R}}]_1\partial[\mathbf{c}_k^{\mathrm{R}}]_2}\\ \dfrac{\partial^2\mathsf{h}_l(\mathbf{c}_k^{\mathrm{R}})}{\partial[\mathbf{c}_k^{\mathrm{R}}]_2\partial[\mathbf{c}_k^{\mathrm{R}}]_1} & \dfrac{\partial^2\mathsf{h}_l(\mathbf{c}_k^{\mathrm{R}})}{\partial[\mathbf{c}_k^{\mathrm{R}}]_2^2}\end{bmatrix}, \tag{38}$$

where

$$\frac{\partial\mathsf{h}_l(\mathbf{c}_k^{\mathrm{R}})}{\partial[\mathbf{c}_k^{\mathrm{R}}]_1} = -2\beta_l^{\mathrm{R}}|C_{k,l}^{\mathrm{R}}|F_l(\sin\vartheta_{\mathrm{R}}^{\mathrm{t}}\sin\varphi_{\mathrm{R}}^{\mathrm{t}}-\sin\vartheta_{\mathrm{R}}^{\mathrm{r}}\sin\varphi_{\mathrm{R}}^{\mathrm{r}})\sum_{j=1}^{J}\sin(F_l(\mathbf{c}_k^{\mathrm{R}}+\mathbf{t}_{k,j}^{\mathrm{R}})^{\mathsf{T}}(\boldsymbol{\rho}_{\mathrm{R}}^{\mathrm{t}}-\boldsymbol{\rho}_{\mathrm{R}}^{\mathrm{r}})-\angle(C_{k,l}^{\mathrm{R}})), \tag{39}$$

$$\frac{\partial\mathsf{h}_l(\mathbf{c}_k^{\mathrm{R}})}{\partial[\mathbf{c}_k^{\mathrm{R}}]_2} = -2\beta_l^{\mathrm{R}}|C_{k,l}^{\mathrm{R}}|F_l(\cos\varphi_{\mathrm{R}}^{\mathrm{t}}-\cos\varphi_{\mathrm{R}}^{\mathrm{r}})\sum_{j=1}^{J}\sin(F_l(\mathbf{c}_k^{\mathrm{R}}+\mathbf{t}_{k,j}^{\mathrm{R}})^{\mathsf{T}}(\boldsymbol{\rho}_{\mathrm{R}}^{\mathrm{t}}-\boldsymbol{\rho}_{\mathrm{R}}^{\mathrm{r}})-\angle(C_{k,l}^{\mathrm{R}})), \tag{40}$$

$$\frac{\partial^2\mathsf{h}_l(\mathbf{c}_k^{\mathrm{R}})}{\partial[\mathbf{c}_k^{\mathrm{R}}]_1^2} = -2\beta_l^{\mathrm{R}}|C_{k,l}^{\mathrm{R}}|(F_l(\sin\vartheta_{\mathrm{R}}^{\mathrm{t}}\sin\varphi_{\mathrm{R}}^{\mathrm{t}}-\sin\vartheta_{\mathrm{R}}^{\mathrm{r}}\sin\varphi_{\mathrm{R}}^{\mathrm{r}}))^2\sum_{j=1}^{J}\cos(F_l(\mathbf{c}_k^{\mathrm{R}}+\mathbf{t}_{k,j}^{\mathrm{R}})^{\mathsf{T}}(\boldsymbol{\rho}_{\mathrm{R}}^{\mathrm{t}}-\boldsymbol{\rho}_{\mathrm{R}}^{\mathrm{r}})-\angle(C_{k,l}^{\mathrm{R}})), \tag{41}$$

$$\frac{\partial^2 \mathsf{h}_l(\mathbf{c}_k^{\mathrm{R}})}{\partial[\mathbf{c}_k^{\mathrm{R}}]_1 \partial[\mathbf{c}_k^{\mathrm{R}}]_2} = -2\beta_l^{\mathrm{R}}|C_{k,l}^{\mathrm{R}}|F_l^2(\sin\vartheta_{\mathrm{R}}^{\mathrm{t}}\sin\varphi_{\mathrm{R}}^{\mathrm{t}} - \sin\vartheta_{\mathrm{R}}^{\mathrm{r}}\sin\varphi_{\mathrm{R}}^{\mathrm{r}})(\cos\varphi_{\mathrm{R}}^{\mathrm{t}} - \cos\varphi_{\mathrm{R}}^{\mathrm{r}}) \times \sum_{j=1}^{J}\cos(F_l(\mathbf{c}_k^{\mathrm{R}} + \mathbf{t}_{k,j}^{\mathrm{R}})^{\mathsf{T}}(\boldsymbol{\rho}_{\mathrm{R}}^{\mathrm{t}} - \boldsymbol{\rho}_{\mathrm{R}}^{\mathrm{r}}) - \angle(C_{k,l}^{\mathrm{R}})), \tag{42}$$

$$\frac{\partial^2 \mathsf{h}_l(\mathbf{c}_k^{\mathrm{R}})}{\partial[\mathbf{c}_k^{\mathrm{R}}]_2 \partial[\mathbf{c}_k^{\mathrm{R}}]_1} = \frac{\partial^2 \mathsf{h}_l(\mathbf{c}_k^{\mathrm{R}})}{\partial[\mathbf{c}_k^{\mathrm{R}}]_1 \partial[\mathbf{c}_k^{\mathrm{R}}]_2}, \tag{43}$$

$$\frac{\partial^2 \mathsf{h}_l(\mathbf{c}_k^{\mathrm{R}})}{\partial[\mathbf{c}_k^{\mathrm{R}}]_2^2} = -2\beta_l^{\mathrm{R}}|C_{k,l}^{\mathrm{R}}|(F_l(\cos\varphi_{\mathrm{R}}^{\mathrm{t}} - \cos\varphi_{\mathrm{R}}^{\mathrm{r}}))^2\sum_{j=1}^{J}\cos(F_l(\mathbf{c}_k^{\mathrm{R}} + \mathbf{t}_{k,j}^{\mathrm{R}})^{\mathsf{T}}(\boldsymbol{\rho}_{\mathrm{R}}^{\mathrm{t}} - \boldsymbol{\rho}_{\mathrm{R}}^{\mathrm{r}}) - \angle(C_{k,l}^{\mathrm{R}})). \tag{44}$$

Since $\mathsf{h}_l(\mathbf{c}_k^{\mathrm{R}})$ has the bounded curvature according to (38) and (41)–(44), we can construct a negative semidefinite matrix $\mathbf{M}_{k,l}^{\mathrm{R}}$ satisfying $\mathbf{M}_{k,l}^{\mathrm{R}} \preceq \nabla_{\mathbf{c}_k^{\mathrm{R}}}^2 \mathsf{h}_l(\mathbf{c}_k^{\mathrm{R}})$. Following the similar procedure of constructing $\mathbf{M}_{m,l}^{\mathrm{B}}$, we directly present $\mathbf{M}_{k,l}^{\mathrm{R}}$ to avoid repetition, which can be expressed as

$$\begin{aligned}\mathbf{M}_{k,l}^{\mathrm{R}} = &-2\beta_l^{\mathrm{R}}|C_{k,l}^{\mathrm{R}}|F_l^2 J(\mathsf{Diag}([(\sin\vartheta_{\mathrm{R}}^{\mathrm{t}}\sin\varphi_{\mathrm{R}}^{\mathrm{t}} - \sin\vartheta_{\mathrm{R}}^{\mathrm{r}}\sin\varphi_{\mathrm{R}}^{\mathrm{r}})^2, (\cos\varphi_{\mathrm{R}}^{\mathrm{t}} - \cos\varphi_{\mathrm{R}}^{\mathrm{r}})^2]^{\mathsf{T}}) \\ &+ |(\sin\vartheta_{\mathrm{R}}^{\mathrm{t}}\sin\varphi_{\mathrm{R}}^{\mathrm{t}} - \sin\vartheta_{\mathrm{R}}^{\mathrm{r}}\sin\varphi_{\mathrm{R}}^{\mathrm{r}})(\cos\varphi_{\mathrm{R}}^{\mathrm{t}} - \cos\varphi_{\mathrm{R}}^{\mathrm{r}})|\mathbf{I}_2).\end{aligned} \tag{45}$$

After replacing $\nabla_{\mathbf{c}_k^{\mathrm{R}}}^2 \mathsf{h}_l(\mathbf{c}_k^{\mathrm{R}})$ in (35) by (45), we obtain a globally concave lower bound of $\mathsf{h}_l(\mathbf{c}_k^{\mathrm{R}})$, which is given by

$$\mathsf{h}_l(\mathbf{c}_k^{\mathrm{R}}|(\mathbf{c}_k^{\mathrm{R}})^{(n)}) = \mathsf{h}_l((\mathbf{c}_k^{\mathrm{R}})^{(n)}) + \nabla_{\mathbf{c}_k^{\mathrm{R}}}^{\mathsf{T}} \mathsf{h}_l(\mathbf{c}_k^{\mathrm{R}})|_{\mathbf{c}_k^{\mathrm{R}}=(\mathbf{c}_k^{\mathrm{R}})^{(n)}}(\mathbf{c}_k^{\mathrm{R}} - (\mathbf{c}_k^{\mathrm{R}})^{(n)}) + (\mathbf{c}_k^{\mathrm{R}} - (\mathbf{c}_k^{\mathrm{R}})^{(n)})^{\mathsf{T}}\frac{\mathbf{M}_{k,l}^{\mathrm{R}}}{2}(\mathbf{c}_k^{\mathrm{R}} - (\mathbf{c}_k^{\mathrm{R}})^{(n)}). \tag{46}$$

Next, we convexify (34c), which can be achieved by utilizing the following first-order Taylor expansion:

$$\|\mathbf{c}_k^{\mathrm{R}} - \mathbf{c}_i^{\mathrm{R}}\|_2 \geqslant \frac{((\mathbf{c}_k^{\mathrm{R}})^{(n)} - \mathbf{c}_i^{\mathrm{R}})^{\mathsf{T}}}{\|(\mathbf{c}_k^{\mathrm{R}})^{(n)} - \mathbf{c}_i^{\mathrm{R}}\|_2}(\mathbf{c}_k^{\mathrm{R}} - \mathbf{c}_i^{\mathrm{R}}). \tag{47}$$

By substituting (46) and (47) into the left hand side of (34a) and that of (34c), respectively, we obtain the following convex optimization problem:

$$(\mathcal{P}6_k): \max_{\mathbf{c}_k^{\mathrm{R}},\kappa} \kappa \tag{48}$$

$$\text{s.t. } \mathsf{h}_l(\mathbf{c}_k^{\mathrm{R}}|(\mathbf{c}_k^{\mathrm{R}})^{(n)}) \geqslant \kappa,\ l \in \mathcal{L}, \tag{48a}$$

$$\mathbf{c}_k^{\mathrm{R}} + \mathbf{t}_{k,j}^{\mathrm{R}} \in \mathcal{C}_{\mathrm{IRS}},\ j \in \mathcal{J}, \tag{48b}$$

$$\frac{((\mathbf{c}_k^{\mathrm{R}})^{(n)} - \mathbf{c}_i^{\mathrm{R}})^{\mathsf{T}}}{\|(\mathbf{c}_k^{\mathrm{R}})^{(n)} - \mathbf{c}_i^{\mathrm{R}}\|_2}(\mathbf{c}_k^{\mathrm{R}} - \mathbf{c}_i^{\mathrm{R}}) \geqslant D_{\mathrm{IRS}},\ i \in \mathcal{K},\ k \neq i, \tag{48c}$$

which can be numerically solved by CVX.

The proposed algorithm for tackling ($\mathcal{P}1$) is summarized in Algorithm 1. In the following, we characterize the complexity of our proposed solution. It can be observed that the complexity of Algorithm 1 is dominated by solving ($\mathcal{P}4_m$) and ($\mathcal{P}6_k$), which result in $\mathcal{O}((L+M)^{1.5})$ and $\mathcal{O}((L+K+J)^{1.5})$ [47], respectively. Therefore, the total complexity of tackling ($\mathcal{P}1$) approximately has an order of $\mathcal{O}(I_{\mathrm{BCD}}(M(L+M)^{1.5} + K(L+K+J)^{1.5}))$, where I_{BCD} denotes the iteration times of handling ($\mathcal{P}1$).

Besides, Theorem 1 elaborates the convergence behavior of our proposed Algorithm 1, whose proof is relegated to Appendix A.

Theorem 1. Assuming that Algorithm 1 starts from a feasible point, the solution iterates generated by Algorithm 1 remain feasible for ($\mathcal{P}1$) and yield monotonically increasing objective values of ($\mathcal{P}1$).

4 Simulation results

In this section, we present numerical results demonstrating the effectiveness of our proposed algorithm and the benefits of deploying an antenna array and an IRS with movable components. Unless otherwise specified, $M = 16$, $K = N$ (i.e., $J = J_1J_2 = 1 \times 1 = 1$), $L = 128$, $f_0 = 287.28$ GHz, $f_L = 291.60$ GHz, $f_{\mathrm{c}} = \frac{f_0+f_L}{2} =$

Algorithm 1 Solution to ($\mathcal{P}1$).

Initialize feasible $\tilde{\mathbf{p}}_{\mathrm{B}}^{(0)}$, $\tilde{\mathbf{c}}_{\mathrm{R}}^{(0)}$ and $n = 0$;
repeat
  for $m = 1$ to M **do**
    Update $(\mathbf{p}_m^{\mathrm{B}})^{(n+1)}$ by solving ($\mathcal{P}4_m$);
  end for
  for $k = 1$ to K **do**
    Update $(\mathbf{c}_k^{\mathrm{R}})^{(n+1)}$ by solving ($\mathcal{P}6_k$);
  end for
  $n := n + 1$;
until convergence.

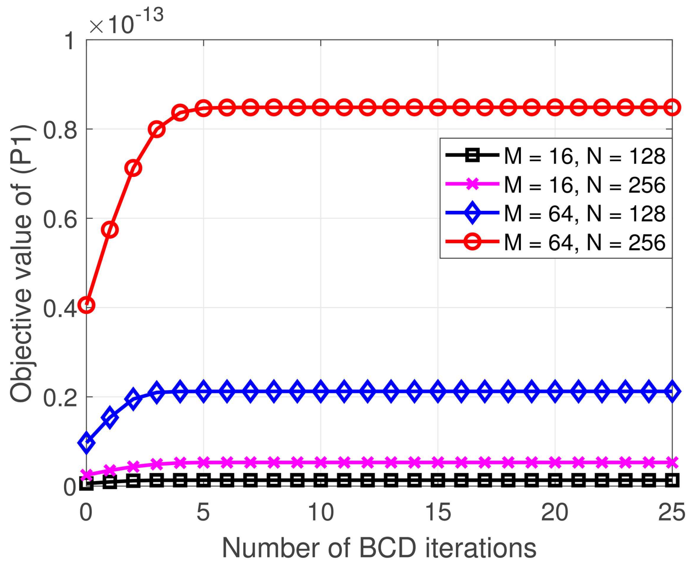

Figure 2 (Color online) Convergence behavior of Algorithm 1.

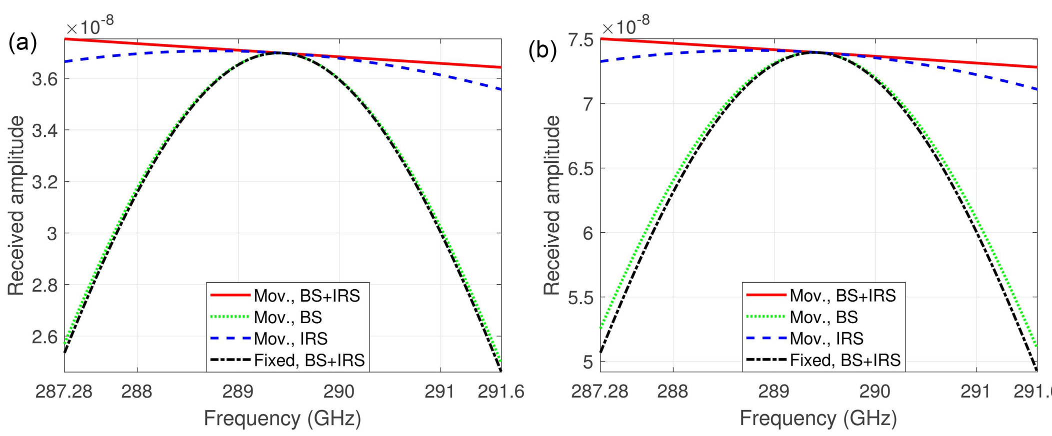

Figure 3 (Color online) Received amplitude across the considered THz frequency band. (a) $N = 128$; (b) $N = 256$.

289.44 GHz [48], $f_l = f_0 + \frac{l}{L}(f_L - f_0)$, $l \in \mathcal{L}$, $A_{\mathrm{BS},1} = A_{\mathrm{BS},2} = \frac{25c}{f_c}$, $A_{\mathrm{IRS},1} = A_{\mathrm{IRS},2} = \frac{50c}{f_c}$, $D_{\mathrm{BS}} = \frac{c}{2f_c}$, $D_{\mathrm{IRS}} = (1 + \sqrt{(J_1-1)^2 + (J_2-1)^2})\frac{c}{2f_c}$, and $\kappa_{\mathrm{abs}}(f_l) = 5.157 \times 10^{-4}$ dB/m.

Figure 2 illustrates the convergence behavior of Algorithm 1. By utilizing Algorithm 1, which starts from feasible initial points, the objective value of ($\mathcal{P}1$) guarantees a monotonically increasing characteristic and converges in several (lower than 10) iterations. This phenomenon coincides with the conclusion drawn by Theorem 1. Furthermore, Figure 2 shows that, after convergence, the objective value of ($\mathcal{P}1$) is at most 109.16% larger than that yielded by the initial point, demonstrating the effectiveness of Algorithm 1. Moreover, with the growth of M and N, the objective value of ($\mathcal{P}1$) increases as the larger array can provide higher beamforming gain.

Figure 3 plots the amplitude of the user's received signal (defined in (9)) across different subcarriers operating

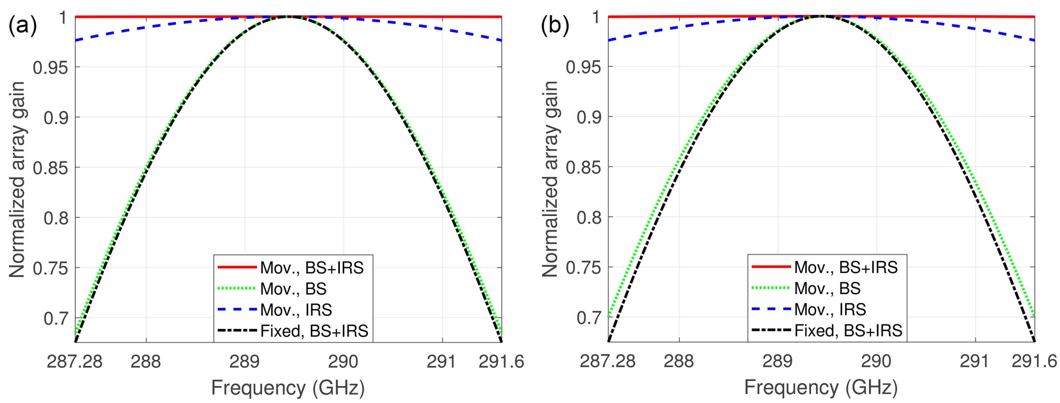

Figure 4 (Color online) Normalized array gain across the considered THz frequency band. (a) $N = 128$; (b) $N = 256$.

in the THz frequency band. The schemes considered in this figure are elaborated as follows.

(i) Mov., BS+IRS: this is our proposed solution, in which BS and IRS are equipped with MAs and movable subarrays, respectively.

(ii) Mov., BS: the antennas at the BS can flexibly move, whereas the IRS elements cannot move.

(iii) Mov., IRS: the BS employs traditional FPAs, whereas the IRS consists of movable subarrays.

(iv) Fixed, BS+IRS: both the BS and IRS are equipped with fixed-position components.

As shown in Figure 3, because the IRS-aided wideband system suffers from a severe double beam squint effect, the amplitudes of the subcarriers at side frequencies degrade significantly when the BS antennas and IRS elements are immobile. This phenomenon underscores the need to incorporate movable components into the BS and IRS. Since the double beam squint effect results from the beam squint at both the BS and IRS, merely moving either the BS antennas or the IRS subarrays cannot sufficiently suppress the double beam squint effect. In contrast, it can be eliminated by appropriately configuring the positions of MAs and subarrays. Furthermore, Figure 3 shows that alleviating beam squint at the IRS is more effective than at the BS. This is because, under the simulation settings, the beam squint effect at the IRS may be more severe than that at the BS, as the IRS is larger than the BS. Besides, with the double beam squint effect mitigated, the received amplitude is not uniform across the considered frequency band. As shown by (9), the received amplitude is related to path loss, whose value becomes smaller when the subcarrier's frequency increases, hence leading to unequal amplitude characteristics. In addition, the received amplitude improves as N increases, thanks to the greater beamforming gain.

Figure 4 depicts the normalized array gain, given by

$$\bar{\mathrm{g}}_l(\tilde{\mathbf{p}}_{\mathrm{B}}, \tilde{\mathbf{c}}_{\mathrm{R}}) = \frac{\mathrm{g}_l^{\mathrm{R}}(\tilde{\mathbf{c}}_{\mathrm{R}})\mathrm{g}_l^{\mathrm{B}}(\tilde{\mathbf{p}}_{\mathrm{B}})}{MN},\ l \in \mathcal{L}, \tag{49}$$

across different subcarriers to more intuitively present the effect of suppressing the double beam squint effect by exploiting MAs at the BS and movable subarrays at the IRS. As shown in Figure 4, because the normalized array gain is independent of the path loss, our proposed solution yields a normalized array gain equal to the theoretical maximum of 1, indicating that the double beam squint effect is successfully eliminated. This phenomenon points out an interesting fact: maximizing the minimal received power is indeed equivalent to maximizing the minimal (normalized) array gain among different subcarriers. Besides, Figure 4 shows that all the curves are symmetric about a central frequency because the normalized array gain does not include path-loss terms. Again, the double beam squint effect cannot be fully mitigated by deploying only an MA array at the BS or by leveraging movable subarrays at the IRS.

Figure 5 shows the impact of the granularity of each IRS subarray on the minimum received power (i.e., the objective value of ($\mathcal{P}1$)). Compared with BS and IRS with fixed-position components, our proposed solution can achieve at least 118.30% and 118.08% higher minimum received power for $N = 128$ and $N = 256$, respectively, significantly enhancing the effectiveness of all subcarriers, especially those far from the central frequency. Besides, Figure 5 shows that the minimum received power deteriorates as the subarray size increases, due to the reduced DoFs in subarray position optimization. Nevertheless, as the subarray size increases from 2×2 to 4×8, the minimum received power degrades by only 0.38% and 0.42% for $N = 128$ and $N = 256$, respectively, which are negligible. This phenomenon provides an essential guideline for practical implementation: appropriately choosing the size of the IRS subarray can significantly reduce hardware costs while ensuring performance requirements. Compared with element-wise movement, which yields the best performance, a movable IRS subarray architecture can reduce the number of

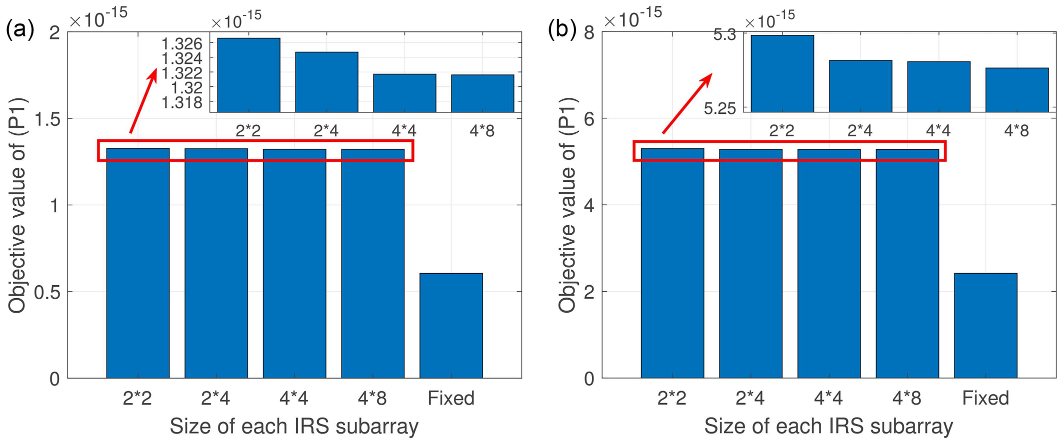

Figure 5 (Color online) Impact of the IRS subarrays' size on the minimum received power. (a) $N = 128$; (b) $N = 256$.

stepper motors, thereby decreasing the power consumption and hardware cost of the entire communication system. Furthermore, the fewer the stepper motors, the lower the signalling overhead, thereby extending the duration of data transmission and making communication more efficient. In addition, as the subarray size increases, the number of optimization variables decreases, which can dramatically reduce computational complexity. Therefore, in practice, it is crucial to strike a balance between system performance and hardware cost by utilizing properly designed IRS subarrays.

5 Conclusion

In this paper, we considered an IRS-aided wideband THz MISO communication system with flexibly movable BS antennas and IRS elements. In particular, the IRS elements are grouped into movable subarrays to reduce power consumption, hardware cost, and computational complexity. To overcome the severe double beam squint effect appearing in the IRS-assisted wideband communication, we formulated a minimum received power maximization problem, where the MAs' and IRS subarrays' positions are jointly configured. By introducing a slack variable, the BCD framework, and the MM methodology, we successfully developed an algorithm to resolve this challenging optimization problem, whose convergence can be mathematically proven. Simulation results verified that the double beam squint effect can be significantly suppressed by adjusting the positions of movable components within the BS and IRS. Moreover, by delicately selecting the size of IRS subarrays, remarkable expenditure reduction with negligible performance degradation can be achieved.

Our proposed double beam squint effect elimination scheme can be straightforwardly applied to multiuser scenarios, although the sum-rate maximization problem (rather than the optimization formulated in this paper) may be considered in light of multiuser interference. Additionally, the recently proposed six-dimensional MA (6DMA) [49] offers greater rotatability than MAs. This merit may further alleviate the double beam squint effect by simultaneously moving BS antennas/IRS elements and rotating the BS array/IRS surface. Furthermore, the collaborative rotation of the BS and IRS to reduce hardware expenditure while satisfying performance requirements is a meaningful problem when the BS and IRS use the 6DMA architecture. In addition, cutting-edge artificial intelligence-based optimization methods can be invoked to tackle the problems in the above-mentioned scenarios, potentially outperforming their traditional counterparts [50]. Currently, these problems remain open and warrant further investigation in future research.

Acknowledgements Qingqing WU's work was supported by National Key R&D Program of China (Grant No. 2023YFB2905000), National Natural Science Foundation of China (Grant No. 62371289), and Shanghai Jiao Tong University 2030 Initiative. Wanming HAO's work was supported by National Natural Science Foundation of China (Grant No. 62471440).

References

1 Shafie A, Yang N, Han C, et al. Terahertz communications for 6G and beyond wireless networks: challenges, key advancements, and opportunities. IEEE Netw, 2023, 37: 162–169
2 Chen Z, Han C, Wu Y, et al. Terahertz wireless communications for 2030 and beyond: a cutting-edge frontier. IEEE Commun Mag, 2021, 59: 66–72
3 Wu Q, Zheng B, You C, et al. Intelligent surfaces empowered wireless network: recent advances and the road to 6G. Proc IEEE, 2024, 112: 724–763
4 Wu Q, Zhang R. Intelligent reflecting surface enhanced wireless network via joint active and passive beamforming. IEEE Trans Wireless Commun, 2019, 18: 5394–5409

5 Huang C, Zappone A, Alexandropoulos G C, et al. Reconfigurable intelligent surfaces for energy efficiency in wireless communication. IEEE Trans Wireless Commun, 2019, 18: 4157–4170
6 Wu Q, Zhang R. Joint active and passive beamforming optimization for intelligent reflecting surface assisted SWIPT under QoS constraints. IEEE J Sel Areas Commun, 2020, 38: 1735–1748
7 Yang Y, Zheng B, Zhang S, et al. Intelligent reflecting surface meets OFDM: protocol design and rate maximization. IEEE Trans Commun, 2020, 68: 4522–4535
8 Zhu J, Huang Y, Wang J, et al. Power efficient IRS-assisted NOMA. IEEE Trans Commun, 2021, 69: 900–913
9 Chu Z, Zhu Z, Zhou F, et al. Intelligent reflecting surface assisted wireless powered sensor networks for Internet of Things. IEEE Trans Commun, 2021, 69: 4877–4889
10 Song X X, Fang Y, Wang F, et al. An overview on IRS-enabled sensing and communications for 6G: architectures, fundamental limits, and joint beamforming designs. Sci China Inf Sci, 2025, 68: 150301
11 Hua M, Wu Q, Chen W, et al. Secure intelligent reflecting surface-aided integrated sensing and communication. IEEE Trans Wireless Commun, 2024, 23: 575–591
12 Wu Q, Chen G, Peng Q, et al. Intelligent reflecting surfaces for wireless networks: deployment architectures, key solutions, and field trials. IEEE Wireless Commun, 2025, 32: 141–148
13 Qiu C, Wu Q, Chen W, et al. Wideband beamforming design for IRS-assisted multi-user THz communications. IEEE Commun Lett, 2025, 29: 269–273
14 Qiu C, Wu Q, Chen W, et al. Beamforming design for intelligent reflecting surface aided near-field THz communications. IEEE Trans Veh Technol, 2026, 75: 1551–1556
15 Ning B, Chen Z, Chen W, et al. Terahertz multi-user massive MIMO with intelligent reflecting surface: beam training and hybrid beamforming. IEEE Trans Veh Technol, 2021, 70: 1376–1393
16 Hao W, Sun G, Zeng M, et al. Robust design for intelligent reflecting surface-assisted MIMO-OFDMA terahertz IoT networks. IEEE Int Things J, 2021, 8: 13052–13064
17 Yan W, Hao W, Huang C, et al. Beamforming analysis and design for wideband THz reconfigurable intelligent surface communications. IEEE J Sel Areas Commun, 2023, 41: 2306–2320
18 Huang C, Yang Z, Alexandropoulos G C, et al. Multi-hop RIS-empowered terahertz communications: a DRL-based hybrid beamforming design. IEEE J Sel Areas Commun, 2021, 39: 1663–1677
19 Saqib N U, Hou S, Chae S H, et al. Reconfigurable intelligent surface aided hybrid beamforming: optimal placement and beamforming design. IEEE Trans Wireless Commun, 2024, 23: 12003–12019
20 Zhu L, Ma W, Mei W, et al. A tutorial on movable antennas for wireless networks. IEEE Commun Surv Tut, 2026, 28: 3002–3054
21 Wong K K, Shojaeifard A, Tong K F, et al. Fluid antenna systems. IEEE Trans Wireless Commun, 2021, 20: 1950–1962
22 Zhu L, Ma W, Zhang R. Movable antennas for wireless communication: opportunities and challenges. IEEE Commun Mag, 2024, 62: 114–120
23 Zhu L, Ma W, Zhang R. Modeling and performance analysis for movable antenna enabled wireless communications. IEEE Trans Wireless Commun, 2024, 23: 6234–6250
24 Ma W, Zhu L, Zhang R. MIMO capacity characterization for movable antenna systems. IEEE Trans Wireless Commun, 2024, 23: 3392–3407
25 Zhu L, Ma W, Ning B, et al. Movable-antenna enhanced multiuser communication via antenna position optimization. IEEE Trans Wireless Commun, 2024, 23: 7214–7229
26 Ma W, Zhu L, Zhang R. Multi-beam forming with movable-antenna array. IEEE Commun Lett, 2024, 28: 697–701
27 Zhu L, Ma W, Xiao Z, et al. Performance analysis and optimization for movable antenna aided wideband communications. IEEE Trans Wireless Commun, 2024, 23: 18653–18668
28 Zhu L, Pi X, Ma W, et al. Dynamic beam coverage for satellite communications aided by movable-antenna array. IEEE Trans Wireless Commun, 2025, 24: 1916–1933
29 Zhu L, Ma W, Xiao Z, et al. Movable antenna enabled near-field communications: channel modeling and performance optimization. IEEE Trans Commun, 2025, 73: 7240–7256
30 Gao Y, Wu Q, Chen W. Joint transmitter and receiver design for movable antenna enhanced multicast communications. IEEE Trans Wireless Commun, 2024, 23: 18186–18200
31 Zheng Z, Wu Q, Chen W, et al. Two-timescale design for movable antenna-enabled multiuser MIMO systems. IEEE Trans Commun, 2025, 73: 10554–10571
32 Zhu Y, Wu Q, Liu Y, et al. Suppressing beam squint effect for near-field wideband communication through movable antennas. IEEE Trans Veh Technol, 2026, 75: 3446–3451
33 Zhong Y, Chen J, Xiao Y, et al. Movable antennas for terahertz broadcast beamforming in hybrid-field scenarios. IEEE Wireless Commun Lett, 2025, 14: 2321–2325
34 Liu K, Wei X, Mei W D, et al. Movable antennas for THz multicasting: grating-lobe analysis and position optimization. Sci China Inf Sci, 2025, 68: 209302
35 Sun Y, Xu H, Ning B, et al. Sum-rate optimization for RIS-aided multiuser communications with movable antennas. IEEE Wireless Commun Lett, 2025, 14: 450–454
36 Wu H, Ren H, Pan C, et al. Movable antenna-enabled RIS-aided integrated sensing and communication. IEEE Trans Cogn Commun Netw, 2025, 11: 2879–2892
37 Ma Y, Liu K, Liu Y, et al. Movable-antenna aided secure transmission for RIS-ISAC systems. IEEE Trans Wireless Commun, 2025, 24: 10019–10035
38 Hu G, Wu Q, Xu D, et al. Intelligent reflecting surface-aided wireless communication with movable elements. IEEE Wireless Commun Lett, 2024, 13: 1173–1177
39 Geng Y, Cheng T H, Zhong K, et al. Joint beamforming and antenna position optimization for IRS-aided multi-user movable antenna systems. IEEE Trans Wireless Commun, 2026, 25: 3750–3765
40 Wu Q, Zhu Y, Peng Q, et al. Intelligent reflecting surfaces for THz communications: fundamentals, key solutions, and system prototyping. 2025. ArXiv:2506.17200v1
41 Sun Y, Babu P, Palomar D P. Majorization-minimization algorithms in signal processing, communications, and machine learning. IEEE Trans Signal Process, 2017, 65: 794–816
42 Bertsekas D. Nonlinear Programming. Belmont: Athena Scientific, 1999
43 Wu Q, Zheng Z, Gao Y, et al. Integrating movable antennas and intelligent reflecting surfaces (MA-IRS): fundamentals, practical solutions, and opportunities. 2025. ArXiv:2506.14636v1
44 Ma W, Zhu L, Zhang R. Compressed sensing based channel estimation for movable antenna communications. IEEE Commun Lett, 2023, 27: 2747–2751
45 Xiao Z, Cao S, Zhu L, et al. Channel estimation for movable antenna communication systems: a framework based on compressed sensing. IEEE Trans Wireless Commun, 2024, 23: 11814–11830
46 Su R, Dai L, Ng D W K. Wideband precoding for RIS-aided THz communications. IEEE Trans Commun, 2023, 71: 3592–3604
47 Ben-Tal A, Nemirovski A. Lectures on Modern Convex Optimization: Analysis, Algorithms, and Engineering Applications. Philadelphia: Society for Industrial and Applied Mathematics, 2001
48 Petrov V, Kurner T, Hosako I. IEEE 802.15.3d: first standardization efforts for sub-terahertz band communications toward 6G. IEEE Commun Mag, 2020, 58: 28–33

49 Shao X, Zhang R. 6DMA enhanced wireless network with flexible antenna position and rotation: opportunities and challenges. IEEE Commun Mag, 2025, 63: 121–128

50 Cui Q M, You X H, Wei N, et al. Overview of AI and communication for 6G network: fundamentals, challenges, and future research opportunities. Sci China Inf Sci, 2025, 68: 171301

Appendix A Proof of Theorem 1

Proof. The feasible domains of $(\tilde{\mathbf{p}}_\mathrm{B}, \tilde{\mathbf{c}}_\mathrm{R})$ corresponding to $(\mathcal{P}1)$ and $(\mathcal{P}2)$ are obviously identical. Suppose that we have obtained a feasible solution $(\tilde{\mathbf{p}}_\mathrm{B}^{(n)}, \tilde{\mathbf{c}}_\mathrm{R}^{(n)}, \kappa^{(n)})$ to $(\mathcal{P}2)$. Via solving $(\mathcal{P}4_1)$, $((\mathbf{p}_1^\mathrm{B})^{(n+1)}, (\mathbf{p}_2^\mathrm{B})^{(n)}, \ldots, (\mathbf{p}_M^\mathrm{B})^{(n)}, \tilde{\mathbf{c}}_\mathrm{R}^{(n)}, \kappa^{(n+\frac{1}{M+K})})$ is obtained (recall $\tilde{\mathbf{p}}_\mathrm{B} \triangleq [(\mathbf{p}_1^\mathrm{B})^\mathsf{T}, \ldots, (\mathbf{p}_M^\mathrm{B})^\mathsf{T}]^\mathsf{T}$) and it is natually a feasible solution to $(\mathcal{P}4_1)$. Since the surrogate functions presented by (31) and (32) are lower bounds of those in $(\mathcal{P}3_1)$, $((\mathbf{p}_1^\mathrm{B})^{(n+1)}, (\mathbf{p}_2^\mathrm{B})^{(n)}, \ldots, (\mathbf{p}_M^\mathrm{B})^{(n)}, \tilde{\mathbf{c}}_\mathrm{R}^{(n)}, \kappa^{(n+\frac{1}{M+K})})$ is also feasible to $(\mathcal{P}3_1)$, so is $(\mathcal{P}2)$, which can be set as a feasible point of $(\mathcal{P}4_2)$. Similarly, after solving $(\mathcal{P}4_2)$, a feasible solution $((\mathbf{p}_1^\mathrm{B})^{(n+1)}, (\mathbf{p}_2^\mathrm{B})^{(n+1)}, (\mathbf{p}_3^\mathrm{B})^{(n)}, \ldots, (\mathbf{p}_M^\mathrm{B})^{(n)}, \tilde{\mathbf{c}}_\mathrm{R}^{(n)}, \kappa^{(n+\frac{2}{M+K})})$ to $(\mathcal{P}2)$ can be acquired, and so forth, $(\tilde{\mathbf{p}}_\mathrm{B}^{(n+1)}, \tilde{\mathbf{c}}_\mathrm{R}^{(n)}, \kappa^{(n+\frac{M}{M+K})})$ is indeed feasible to $(\mathcal{P}2)$, which implies that $(\tilde{\mathbf{p}}_\mathrm{B}^{(n+1)}, \tilde{\mathbf{c}}_\mathrm{R}^{(n)}, \kappa^{(n+\frac{M}{M+K})})$ is also feasible to $(\mathcal{P}6_1)$. Following similar arguments, we can conclude that, by sequentially solving $(\mathcal{P}6_1)$ to $(\mathcal{P}6_K)$, $(\tilde{\mathbf{p}}_\mathrm{B}^{(n+1)}, \tilde{\mathbf{c}}_\mathrm{R}^{(n+1)}, \kappa^{(n+1)})$ is feasible to $(\mathcal{P}2)$, so is $(\mathcal{P}1)$. Hence, we have proven that the solution iterates remain feasible.

Furthermore, we have

$$\begin{aligned}
\min_{l\in\mathcal{L}} \mathsf{h}_l(\tilde{\mathbf{p}}_\mathrm{B}^{(n+1)}, \tilde{\mathbf{c}}_\mathrm{R}^{(n+1)}) &\overset{(a)}{\geqslant} \min_{l\in\mathcal{L}} \mathsf{h}_l(\tilde{\mathbf{p}}_\mathrm{B}^{(n+1)}, (\mathbf{c}_1^\mathrm{R})^{(n+1)}, \ldots, (\mathbf{c}_K^\mathrm{R})^{(n+1)} | (\mathbf{c}_K^\mathrm{R})^{(n)}) \overset{(b)}{=} \kappa^{(n+1)} \overset{(c)}{\geqslant} \kappa^{(n+\frac{M+K-1}{M+K})} \\
&\overset{(d)}{=} \min_{l\in\mathcal{L}} \mathsf{h}_l(\tilde{\mathbf{p}}_\mathrm{B}^{(n+1)}, (\mathbf{c}_1^\mathrm{R})^{(n+1)}, \ldots, (\mathbf{c}_{K-1}^\mathrm{R})^{(n+1)}, (\mathbf{c}_K^\mathrm{R})^{(n)} | (\mathbf{c}_K^\mathrm{R})^{(n)}) \\
&\overset{(e)}{=} \min_{l\in\mathcal{L}} \mathsf{h}_l(\tilde{\mathbf{p}}_\mathrm{B}^{(n+1)}, (\mathbf{c}_1^\mathrm{R})^{(n+1)}, \ldots, (\mathbf{c}_{K-1}^\mathrm{R})^{(n+1)}, (\mathbf{c}_K^\mathrm{R})^{(n)}) \\
&\overset{(f)}{\geqslant} \min_{l\in\mathcal{L}} \mathsf{h}_l(\tilde{\mathbf{p}}_\mathrm{B}^{(n+1)}, \tilde{\mathbf{c}}_\mathrm{R}^{(n)}) \overset{(g)}{\geqslant} \min_{l\in\mathcal{L}} \mathsf{h}_l(\tilde{\mathbf{p}}_\mathrm{B}^{(n)}, \tilde{\mathbf{c}}_\mathrm{R}^{(n)}),
\end{aligned} \tag{A1}$$

where (a) holds since $\mathsf{h}_l(\tilde{\mathbf{p}}_\mathrm{B}, \mathbf{c}_1^\mathrm{R}, \ldots, \mathbf{c}_K^\mathrm{R} | (\mathbf{c}_K^\mathrm{R})^{(n)})$ is a lower bound of $\mathsf{h}_l(\tilde{\mathbf{p}}_\mathrm{B}, \tilde{\mathbf{c}}_\mathrm{R})$ (refer to (46)) and $\tilde{\mathbf{c}}_\mathrm{R} \triangleq [(\mathbf{c}_1^\mathrm{R})^\mathsf{T}, \ldots, (\mathbf{c}_K^\mathrm{R})^\mathsf{T}]^\mathsf{T}$. When $(\mathcal{P}6_K)$ gets solved, one key observation is that at least one of the $(L+1)$ constraints in (48a) achieves equalities following the fact that the objective (48) is linear in κ, which implies the equality (b). The inequality (c) stands because the update of $\mathbf{c}_K^\mathrm{R}$ by solving $(\mathcal{P}6_K)$ increases the objective. Due to the feasibility of $(\tilde{\mathbf{p}}_\mathrm{B}^{(n+1)}, (\mathbf{c}_1^\mathrm{R})^{(n+1)}, \ldots, (\mathbf{c}_{K-1}^\mathrm{R})^{(n+1)}, (\mathbf{c}_K^\mathrm{R})^{(n)}, \kappa^{(n+\frac{M+K-1}{M+K})})$ with the setting $\kappa^{(n+\frac{M+K-1}{M+K})} = \min_{l\in\mathcal{L}} \mathsf{h}_l(\tilde{\mathbf{p}}_\mathrm{B}^{(n+1)}, (\mathbf{c}_1^\mathrm{R})^{(n+1)}, \ldots, (\mathbf{c}_{K-1}^\mathrm{R})^{(n+1)}, (\mathbf{c}_K^\mathrm{R})^{(n)} | (\mathbf{c}_K^\mathrm{R})^{(n)})$, we obtain (d), and (e) follows since the functions $\mathsf{h}_l(\tilde{\mathbf{p}}_\mathrm{B}^{(n+1)}, (\mathbf{c}_1^\mathrm{R})^{(n+1)}, \ldots, (\mathbf{c}_{K-1}^\mathrm{R})^{(n+1)}, (\mathbf{c}_K^\mathrm{R})^{(n)})$ and $\mathsf{h}_l(\tilde{\mathbf{p}}_\mathrm{B}^{(n+1)}, (\mathbf{c}_1^\mathrm{R})^{(n+1)}, \ldots, (\mathbf{c}_{K-1}^\mathrm{R})^{(n+1)}, (\mathbf{c}_K^\mathrm{R})^{(n)} | (\mathbf{c}_K^\mathrm{R})^{(n)})$ coincide at the point $(\mathbf{c}_K^\mathrm{R})^{(n)}$. Lastly, (f) is concluded from repeating similar procedures (a)–(e), and (g) can also be obtained similarly, which proves that the objective value monotonically increases. Due to the objective value of $(\mathcal{P}1)$ evidently upper-bounded by $\min_{l\in\mathcal{L}} \alpha_{\mathrm{G},l}^2 \alpha_{\mathrm{h},l}^2 M^2 N^2$, the objective sequence converges.